Ore Geology Reviews 88 (2017) 718–738

Contents lists available at ScienceDirect

Ore Geology Reviews

journal homepage: www.elsevier.com/locate/oregeorev

Highly fractionated Early Cretaceous I-type granites and related Sn polymetallic mineralization in the Jinkeng deposit, eastern Guangdong, SE China: Constraints from geochronology, geochemistry, and Hf isotopes

Zengwang Qiu [a,b], Qinghe Yan [a,b], Shasha Li [a,b], He Wang [a,*], Laixi Tong [a], Rongqing Zhang [a], Xiaopeng Wei [a,b], Pei Li [a,b], Liming Wang [c], An Bu [d], Lunming Yan [d]

[a] Key Laboratory of Mineralogy and Metallogeny, Guangzhou Institute of Geochemistry, Chinese Academy of Sciences, Guangzhou 510640, China
[b] University of Chinese Academy of Sciences, Beijing 100049, China
[c] Geology Bureau for Nonferrous Metals of Guangdong Province, Guangzhou 510060, China
[d] Geology Bureau for Nonferrous Metals of Guangdong Province, 931 Team, Shantou 515041, China

ARTICLE INFO

Article history:
Received 24 March 2016
Received in revised form 7 October 2016
Accepted 11 October 2016
Available online 17 October 2016

Keywords:
Jinkeng
Sn-bearing granites
Geochronology
Geochemistry
Hf isotopes
Eastern Guangdong

ABSTRACT

The recently discovered Jinkeng deposit, located in eastern Guangdong Province, SE China, is a granite-related cassiterite–sulfide-type Sn–Cu–Pb–Zn deposit in the Cathaysia Block. Zircon U–Pb dating of the biotite granite and fine-grained granite associated with the deposit yielded concordant ages of 144.7 ± 0.8 Ma and 141.1 ± 1.3 Ma, respectively. These ages are consistent, within error, with the molybdenite Re–Os isochron age of 139.3 ± 2.5 Ma for the deposit, indicating a temporal link between the emplacement of granitic plutons and polymetallic Sn mineralization. Combined with the regional mineralization ages, we propose that the 145–135 Ma interval represents another significant period of Sn–W mineralization in southern China, in addition to those already recognized. The biotite granite and fine-grained granite have similar geochemical characteristics; both are weakly peraluminous, high-K and calc-alkaline, containing abundant Si, Na, and K, and low concentrations of Fe, Mg, Ca, and P. Compared to primitive mantle and unfractionated granitoids, they are enriched in Rb, Th, U, K, and Pb, have relatively high Rb/Sr and low K/Rb values, are depleted in Ba, Sr, and Ti, and have prominent negative Eu anomalies (δEu = 0.05–0.19), characteristic of highly fractionated I-type granites. Zircons from these granites have $\varepsilon_{Hf}(t)$ values ranging from −9.2 to −3.3, and Hf model ages (T_{DM2}) of 1776–1406 Ma, suggesting that the granites formed by the partial melting of Proterozoic basement material, and contain a minor mantle-derived component. Highly fractionated and reduced (fO_2 below NNO) magma facilitated the enrichment of Sn. Existing knowledge on the tectonic evolution of this region and new data from this study, indicate that the granites and associated Sn mineralization in the Jinkeng deposit formed in an extensional environment at ~140 Ma, likely related to the rollback of the paleo-Pacific Plate.

1. Introduction

Sn deposits are commonly associated with granites rich in volatile elements (e.g., F, B, and Li), which formed from highly fractionated, reduced magmas (Blevin and Chappell, 1995; Breiter, 2012; Feng et al., 2012; Fogliata et al., 2012; Heinrich, 1990; Lehmann and Harmanto, 1990; Wang et al., 2013; Xu et al., 2016), such as Mesozoic granitoids in southern China that were generated during the subduction of the paleo-Pacific Plate beneath the South China Block (Charvet et al., 1994; Hu and Zhou, 2012; Lapierre et al., 1997; Li and Li, 2007; Mao et al., 2004, 2008, 2013a; Zhou and Li, 2000; Zhou et al., 2006). Mesozoic Sn–W deposits are abundant in the Nanling and adjacent areas, and are intimately associated with the widespread granitoids. These deposits were formed during three episodes during the Late Triassic (230–210 Ma), Late Jurassic (160–150 Ma), and Cretaceous (134–80 Ma; Chen et al., 2008; Hu and Zhou, 2012; Mao et al., 2013a). In contrast, few 145–135 Ma Sn–W deposits have been discovered in southern China (Mao et al., 2008, 2013a); those identified include the Tiandong W–Sn (Li et al., 2016; Liu et al., 2015) and Taoxihu (Qiu et al., 2016a) and Jinkeng Sn polymetallic deposits (Li et al., 2012) in eastern Guangdong in coastal southeastern China.

Eastern Guangdong Province is located at the junction of the E–W-trending Nanling tectono-magmatic belt, and the NE–SW-trending Coastal Magmatic Belt in the Cathaysia Block (Fig. 1). The area contains abundant Sn–W polymetallic deposits, which are related to Mesozoic

* Corresponding author.
E-mail address: wanghe@gig.ac.cn (H. Wang).

http://dx.doi.org/10.1016/j.oregeorev.2016.10.008
0169-1368/

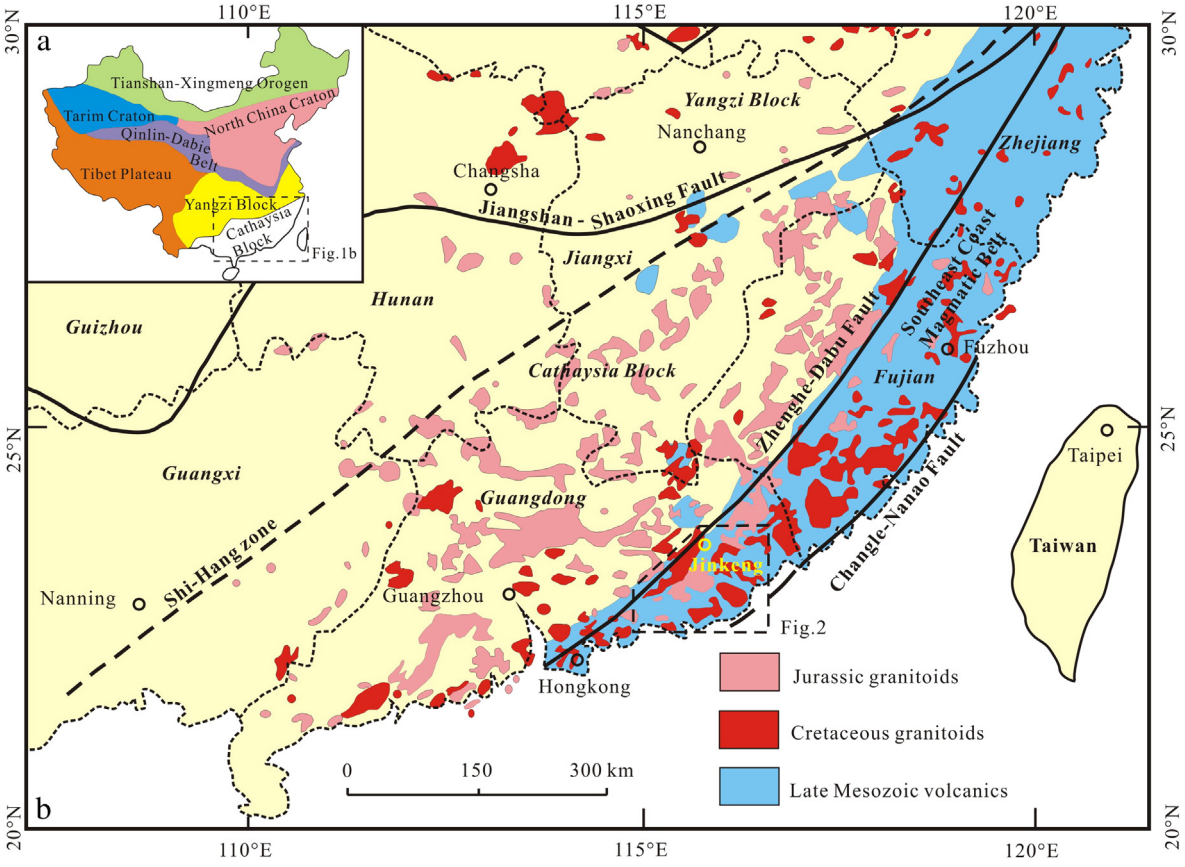

Fig. 1. (a) Tectonic map of China and (b) simplified geological map showing the distribution of Mesozoic granitoids and volcanics within the South China Craton. (modified from Zhou et al., 2006).

granitoids and volcanic rocks, and include the Tashan, Changpu, Jishuimen, Xiling, Houpo'ao, and Lianhuashan deposits. Although these deposits were extensively studied throughout the 1980s and 1990s (Ni et al., 1983; Xu, 1993; Xu and Yue, 1999a), they remain poorly understood compared with other regions in southern China due to mine closures over the last decade. The recent discovery of new Sn–W deposits in the region has renewed interest in these mineral systems and associated granites.

The Jinkeng Sn deposit occurs along the northeastern section of the Lianhuashan Fault, which represents an extension of the Zhenghe–Dabu regional fault system in eastern Guangdong Province. It is a hydrothermal cassiterite–sulfide vein-type Sn–Cu–Pb–Zn deposit containing 110,807 t Cu, 7809 t Sn, 26,552 t Pb, 147,493 t Zn, at average grades of 0.68% Cu, 1.43% Pb, 1.68% Zn, and 0.29% Sn (GNMGB, 2015). Li et al. (2012) suggested that the mineralization is associated with the granites surrounding the deposit, although little is known about the geology of the area, timing of the mineralization, or genesis of the deposit itself. Here, we present the first systematic study of the geology, zircon U–Pb and molybdenite Re–Os geochronology, geochemistry, and Lu–Hf isotopic compositions of the mineralization-related granites of the Jinkeng deposit. We use these data to constrain the age, petrogenesis, source, and tectonic setting of the deposit, and to identify a significant period of W–Sn metallogenesis from 145 to 135 Ma in southern China.

2. Regional geology

The geology of eastern Guangdong is dominated by a suite of clastic littoral and shallow-marine facies sedimentary rocks of the Upper Triassic Xiaoping and Lower Jurassic Jinji formations, rhyolitic tuffs and lavas of the Upper Jurassic Gaojiping Formation, and red bed and tuffaceous clastic sediments of the Lower Cretaceous Guancaohu Formation (Fig. 2; Xu and Yue, 1999a; Xu et al., 2000). The principal structures in this area are NE–SW- and NW–SE-trending faults as well as minor E–W-trending faults. Three sub-parallel regional NE–SW-trending fault systems occur; from west to east, these are the Lianhuashan, Puning–Chaozhou, and Huilai–Raoping faults. They have imposed a structural control on the distribution of Mesozoic granitoids, volcanic rocks, and associated ore deposits in the region, in particular the Changpu–Jinkeng, Xiling–Houpoao, and Zhongqiuyang–Lianhuashan Sn–W belts (Fig. 2; Xu and Yue, 1999a). Mesozoic (Middle Jurassic to Early Cretaceous) granitoids are abundant in the area, and include biotite granites, monzogranites, and granodiorites. Massive coeval volcanic and sub-volcanic rocks are also present along the regional faults, or within rift basins such as the Early Cretaceous Guancaohu Basin (Guo and Bu, 2006). Earlier research suggests that both the granitoids and volcanic rocks belong to a suite of transitional I- and S-type felsic rocks (Xu et al., 2000).

The Changpu–Jinkeng Sn polymetallic belt is structurally controlled by the Lianhuashan Fault, and is located in the western part of eastern Guangdong Province in an area dominated by sandstones of the Upper Triassic Xiaoping Formation, shaly sandstones of the Lower Jurassic Jinji Formation, and volcanic rocks of the Upper Jurassic Gaojiping Formation. The volcanic successions comprise tuffs, ignimbrites, dacites, and rhyolites, and the plutonic suite includes biotite granites and monzogranites. The Lianhuashan Fault system in the study area is characterized by progressive low- to medium-pressure metamorphism preserved as ENE-trending sericite–phyllite, garnet–two-mica-schist, and staurolite–andalusite-schist belts, and strike-slip ductile shear zones (Qiu et al., 1991). More than 50 ore deposits have been discovered in the region, including the Jinkeng, Taoxihu, Tashan, Dadaoshan, Changpu, and Jishuimen Sn polymetallic deposits, and the Baxiang Fe deposit.

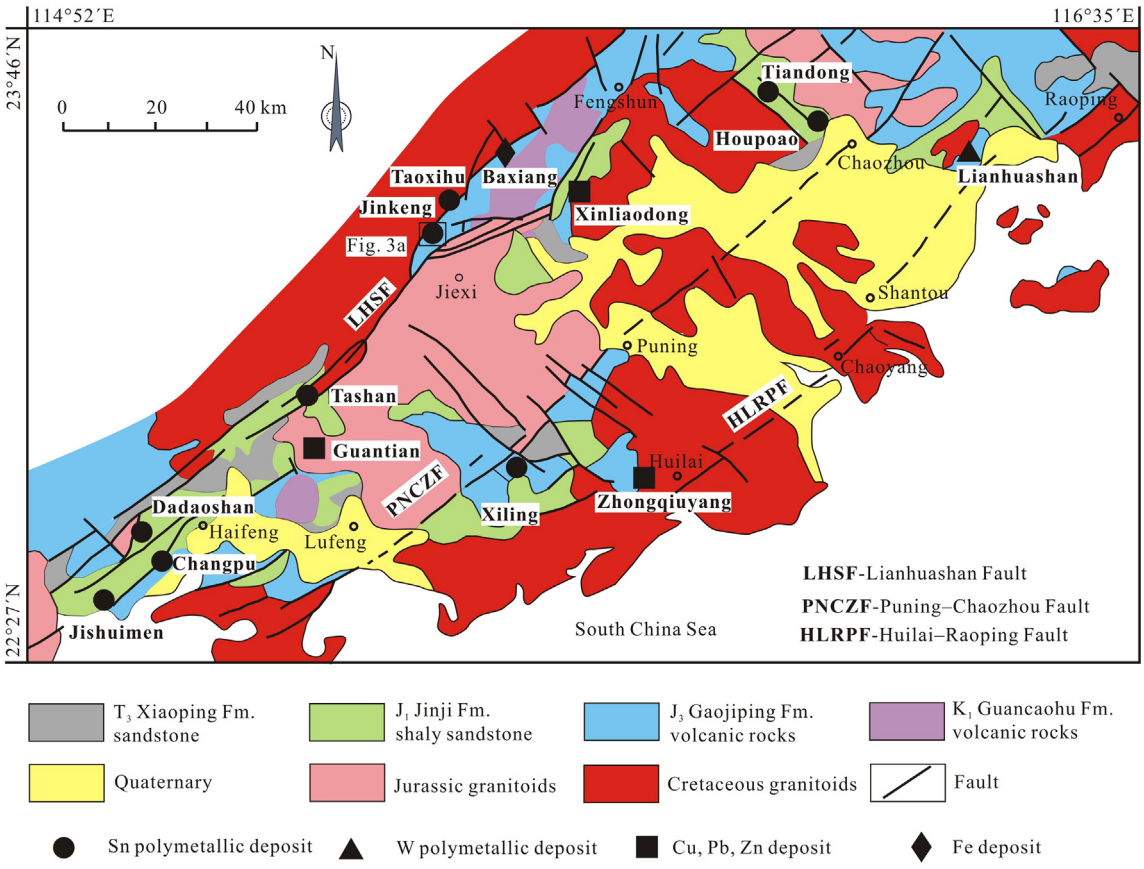

Fig. 2. Geological map of eastern Guangdong Province. (modified after Xu and Yue, 1999a).

3. Geology of the Jinkeng Sn polymetallic deposit

The Jinkeng deposit is located in the northeastern part of the Lianhuashan Sn Belt (115°45′00″–115°48′45″E, 23°28′00″–23°32′00″ N), within the garnet–two-mica-schist belt (Qiu et al., 1991; Fig. 2). The geology of the study area comprises volcanic successions of the Upper Jurassic Gaojiping Formation, and Quaternary cover (Fig. 3). The volcanic suite includes silicic lava, dacite, rhyolite, and tuff units, striking NE–SW, and dipping 20°–40° SE. The intrusive rocks are silicic and intermediate, and include medium- to coarse-grained biotite granite (hereafter referred to as the biotite granite), fine-grained granite, and porphyritic granodiorite (Fig. 3). The biotite granite and fine-grained granite show gradational contacts, and are interpreted to be the inner and marginal facies, respectively, of a granitic pluton that intrudes the porphyritic granodiorite and the Gaojiping Formation.

Mineralization in the Jinkeng deposit occurs in the Mashan and Kongjiao ore blocks (Fig. 3). The orebodies are associated with NE–SW-, NW–SE-trending faults which controlled mineralization, and N–S-trending faults, which post-date ore deposition. The NE–SW-trending faults are pervasive throughout the study area, and are structurally influenced by the regional Lianhuashan Fault system, striking 10°–40°, and dipping 30°–50° SE. They control the distribution of mineralization in the Mashan ore block (Figs. 3 and 4a). The NW–SE-trending faults strike 290°–330°, dip 25°–60° NE, are located within the porphyritic granodiorite, and control the distribution of mineralized veins in the Kongjiao ore block (Figs. 3 and 4b). Almost all of the NE–SW- and NW–SW-trending structures exhibit evidence of compressional to tensional deformation, which may have generated space for ore deposition, and influenced the size of the orebodies. The volcanic rocks of the Gaojiping Formation, and the porphyritic granodiorite in the study area have been significantly affected by regional metamorphism and dynamothermal metamorphism, which produced garnet–sericite–biotite schist locally within the Gaojiping Formation. However, the biotite and fine-grained granites are weakly deformed, indicating that the majority of the sinistral strike-slip shearing within the Lianhuashan system predates their emplacement.

Veins are developed in the Mashan ore block, and are typically hosted in NE–SW- to NNE–SW-trending cleavage planes and fractures in the Gaojiping Formation outside the contact zone with the fine-grained granite (Fig. 5a). Mineralization in the Mashan block occurs in a 1500 m long, 50–200 m wide, and 1200 m deep area. The block contains over 30 NE–SW-trending (15°–40°) veins, dipping 25°–60° SE, measuring 10–1300 m long, 0.1–2.7 m thick, and extending to depths of 450–1000 m. The V_1 orebody is 800 m long and 2.7 m thick, and extends to a depth of 435 m; its average ore grade is 1.39% Cu, 0.22% Sn, 0.83% Pb, and 0.79% Zn. The V_4 orebody is 1000 m long and 0.1–1.2 m thick, extends to a depth of 200 m, and contains 0.70% Cu, 0.10% Sn, 0.34% Pb, and 0.99% Zn. Veins in the Kongjiao ore block are structurally controlled by NW–SE-trending faults crosscutting the porphyritic granodiorite outside of the fine-grained granite intrusion. Mineralization in this block occurs in an area 600 m long and 80–150 m thick, extending to a depth of 250 m. Six main ore veins have been identified, and they strike NW–SE (295°–330°) and dip 25°–60° NE. Individual veins are typically 150–600 m long and 0.5–1.6 m thick, and extend to a depth of 70–250 m. The V_5 orebody is the most economically significant orebody in the deposit, measuring 600 m long, with an average thickness of 1.75 m, extending to a depth of 250 m, and containing 0.59% Cu, 0.23% Sn, 1.76% Pb, and 4.42% Zn. These veins pinch and swell, and occur as lenticular, branching, and combined structures.

Mineralization in the Mashan and Kongjiao ore blocks is similar, and is characterized by quartz–silicate veins containing cassiterite and sulfides (Fig. 5). The ore minerals are predominantly subhedral and

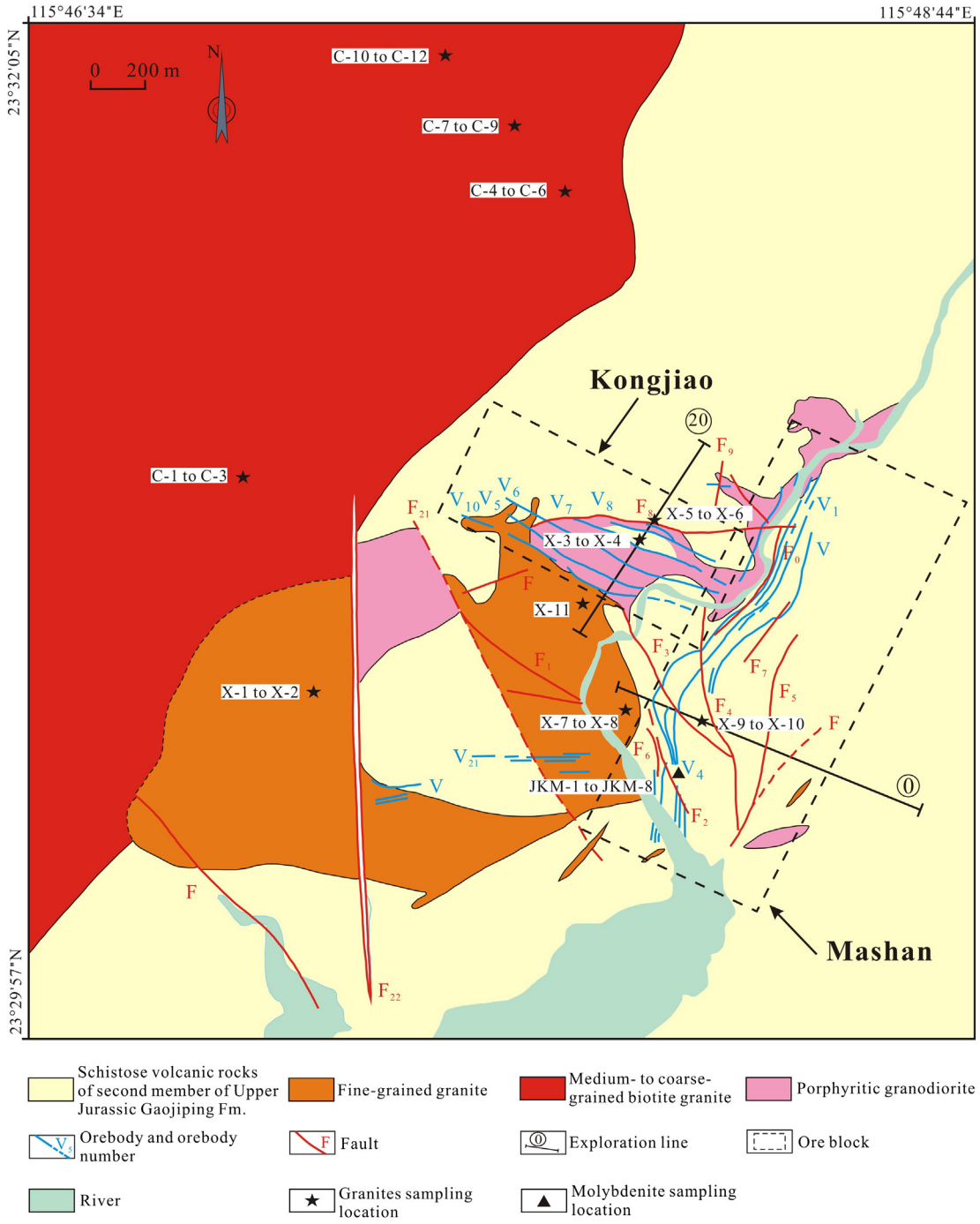

Fig. 3. Simplified geological map of the Jinkeng Sn polymetallic deposit (modified after Guangdong Nonferrous Metals Geological Bureau 931 Team, 2015). Sampling locations for the Jinkeng granites and molybdenite are shown on the figure, with the sample numbers C-1 and X-1 are abbreviations for 15JKC-1 and 15JKX-1, respectively. This also applies to other sample numbers of granites. Biotite granite: 23°31′15″N/115°47′12″E (C-1 to C-3), 23°31′37″N/115°47′53″E (C-4 to C-6), 23°31′51N/115°47′42″E (C-7 to C-9) and 23°32′03″N/115°47′32″E (C-10 to C-12). Fine-grained granite: 23°30′41″N/115°47′14″E (X-1 to X-2), 23°31′00″N/115°47′59″E (X-3 to X-4), 23°31′03″N/115°48′01″E (X-5 to X-6), 23°30′39″N/115°47′57″E (X-7 to X-8), 23°30′39″N/115°48′07″E (X-9 to X-10) and 23°30′50″N/115°47′53″E (X-11). Molybdenite: 23°30′35″N/115°48′09″E (JKM-1 to JKM-8).

anhedral, and show various replacement textures (Fig. 6). Chalcopyrite occurs as blebs within sphalerite (Fig. 6e), and replaces arsenopyrite or pyrite along grain margins (Fig. 6d, e). Chalcopyrite and sphalerite also replace arsenopyrite along fractures (Fig. 6c). The main ore minerals include cassiterite, pyrite, arsenopyrite, pyrrhotite, chalcopyrite, sphalerite, and galena, with minor molybdenite and native silver (Fig. 6). Gangue minerals include quartz, biotite, muscovite, sericite, chlorite, and calcite (Fig. 6a, g, h).

Hydrothermal alteration is widespread in the Jinkeng deposit; alteration types include silicification, biotitization, muscovitization, chloritization, which are closely associated with cassiterite mineralization, and carbonatization. Biotitization and muscovitization are developed along the contact between granite and the walk rock where quartz–cassiterite–arsenopyrite orebodies occur (Figs. 5a–b and 6a). Silicification is the most common alteration type, and occurs as veins and coarse-grained quartz coexisting with metallic minerals (Figs. 5 and 6a, g, h) developed near orebodies along faults or fractures. Chloritization is characterized by chlorite veins that are extensively developed near orebodies in the crush deformation zones. The chlorite is intergrown with muscovite, and both replace biotite (Figs. 5c and 6g).

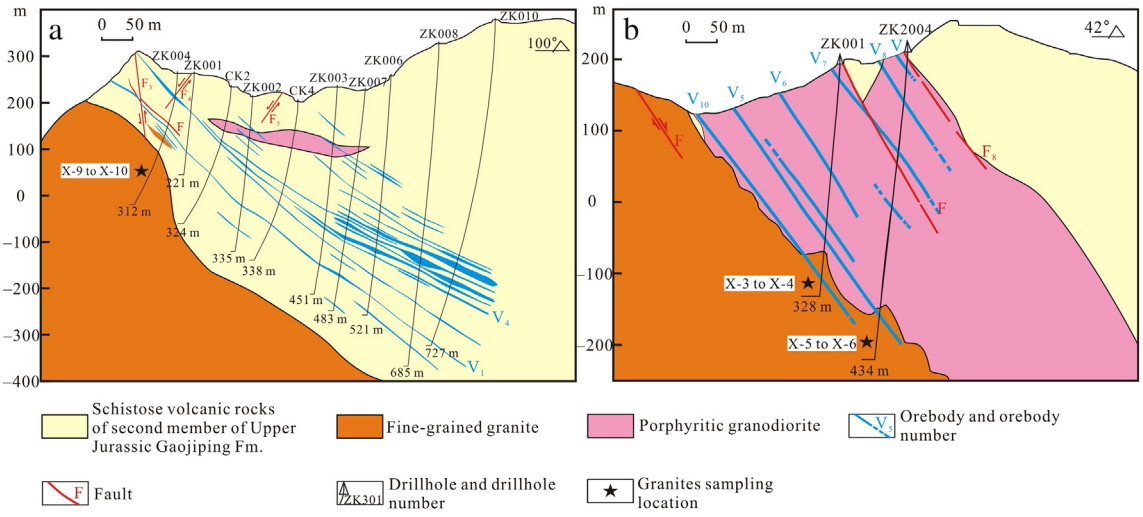

Fig. 4. Geological cross-sections along exploration lines (a) No. 0 and (b) No. 20 of the Jinkeng Sn polymetallic deposit showing the distribution of ore bodies.

Carbonatization occurs as calcite veins coexisting with Pb–Zn–(Cu) orebodies in the late mineralization stage (Figs. 5d and 6h). Although garnet occurs in the deposit, it is typically crushed and deformed, and appears as asymmetric rotated porphyroclasts, filled and replaced along fractures by quartz, biotite, chlorite, or sulfides. We propose that the garnet was formed during the regional and dynamothermal metamorphic events prior to mineralization.

Based on field observation and microscopy work, we propose that hypogene mineralization occurred in three paragenetic stages. The early, quartz–biotite–cassiterite–arsenopyrite stage is characterized by the crystallization of cassiterite, euhedral to subhedral arsenopyrite, and pyrite with minor molybdenite, coexisting with quartz, biotite, and muscovite (Figs. 5b and 6a, b). This stage of mineralization is developed in the inner and outer contact zones of the granite body. The main quartz–chlorite–cassiterite–sulfide stage consists of cassiterite, pyrrhotite, pyrite, chalcopyrite, sphalerite, and galena, coexisting with quartz, muscovite, and chlorite (Figs. 5c and 6e–g). This stage is developed in the interbed faults of the Gaojiping volcanic rocks, and the porphyritic granodiorite outside the contact zones of the granites. The mineral assemblages of this stage commonly replace or crosscut earlier minerals (Fig. 6c, d). Late stage mineralization is characterized by quartz–calcite–sulfide assemblages, consisting of pyrite, sphalerite, galena, chalcopyrite, and native silver, coexisting with quartz and calcite (Figs. 5d and 6h). The quartz–calcite–sulfide veins occur distal to the granite, and

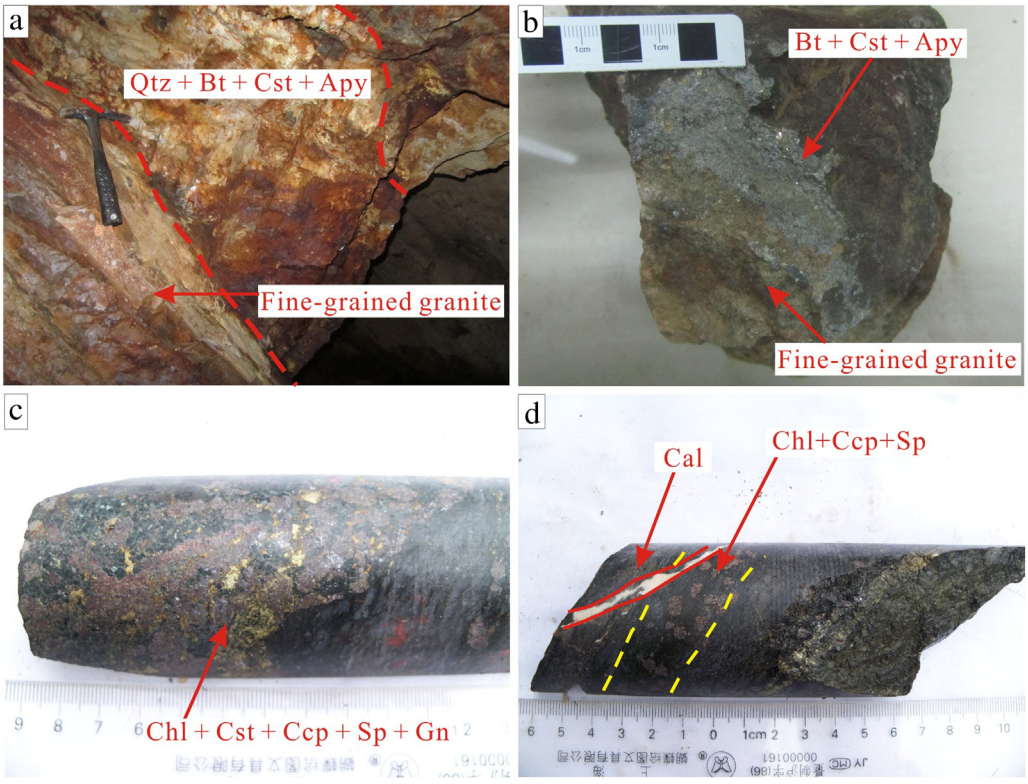

Fig. 5. Representative photographs showing variations in mineralization within the Jinkeng Sn polymetallic deposit. (a) Veined mineralization developed within a crushed zone along the contact between the fine-grained granite and the Gaojiping Formation. (b) Massive quartz–arsenopyrite–cassiterite ore. (c) Veined–disseminated chlorite–sphalerite–galena–chalcopyrite–cassiterite ore. (d) Calcite vein cross-cutting the former chlorite–sphalerite–galena–chalcopyrite–cassiterite ore. Cst = cassiterite, Apy = arsenopyrite, Ccp = chalcopyrite, Sp = sphalerite, Gn = galena, Qtz = quartz, Bt = biotite, Chl = chlorite.

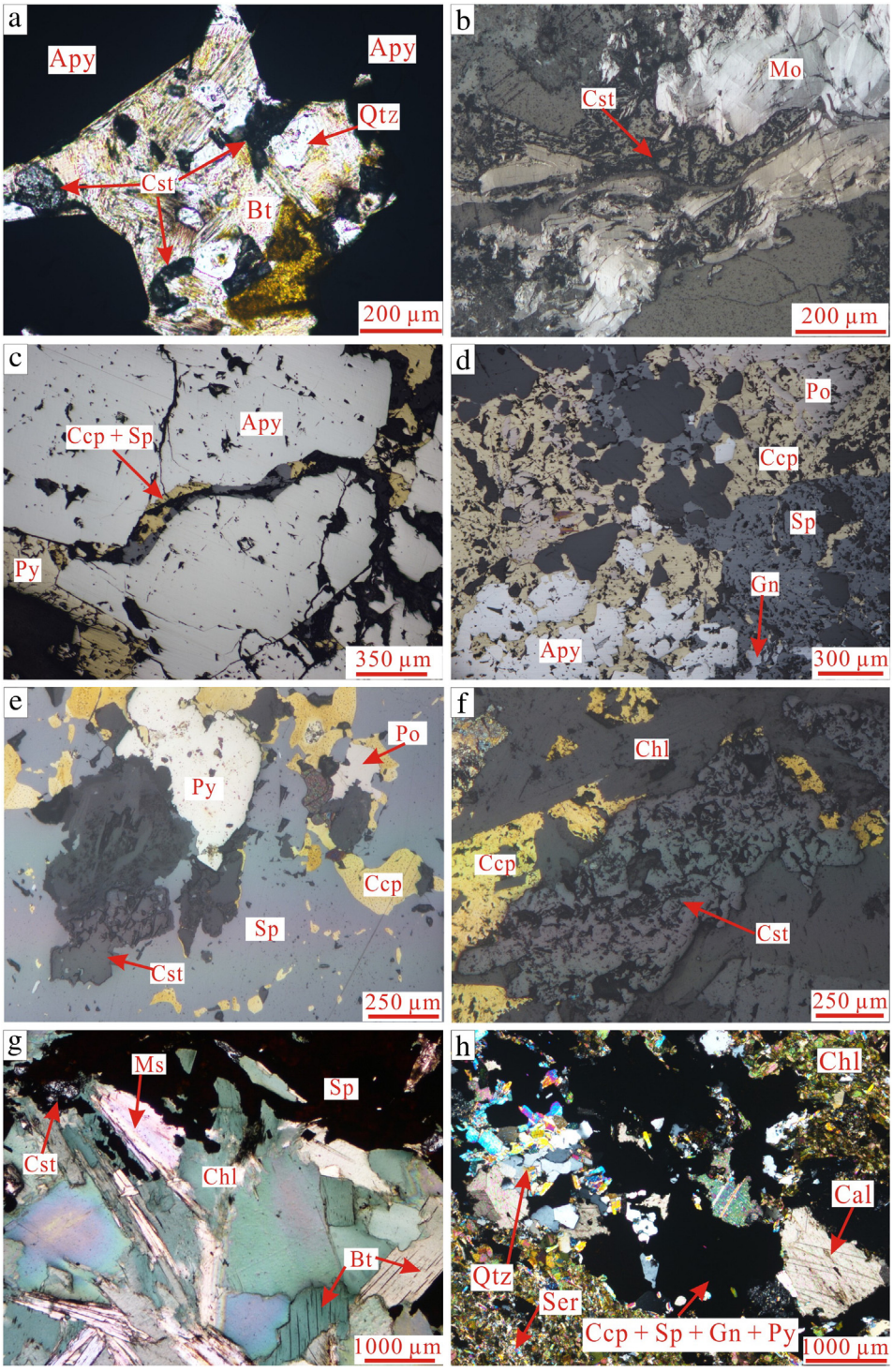

Fig. 6. Representative photomicrographs taken under reflected light (b–f), under plane polarized light (a), and cross polarized light (g and h) showing variations in mineralization within the Jinkeng Sn polymetallic deposit. (a) Arsenopyrite and cassiterite intergrown with biotite and quartz. (b) Molybdenite coexisting with cassiterite. (c) Arsenopyrite cross-cut by chalcopyrite and sphalerite vein. (d) Arsenopyrite surrounded and replaced by pyrrhotite, chalcopyrite and shpalerite. (e) Cassiterite coexisting with chalcopyrite, sphalerite, and pyrrhotite. (f) Cassiterite coexisting with chalcopyrite. (g) Sphalerite and cassiterite coexisting with chlorite and muscovite; the chlorite and muscovite replaced the early stage biotite. (h) Quartz-calcite-sulfide vein cross-cut the chlorite of former stage. Py = pyrite, Mo = molybdenite, Po = pyrrhotite, Ser = sericite, Ms. = muscovite, and other abbreviations are the same as Fig. 5.

crosscut main stage chlorite–cassiterite–sulfide orebodies (Figs. 5d and 6h).

Zonation of alteration and mineralization is observed, with quartz–biotite–cassiterite–arsenopyrite (Sn–As) occurring proximal to the granite, followed by quartz–chlorite–cassiterite–sulfide (Sn–Cu–Pb–Zn), and quartz–calcite–sulfide (Pb–Zn) distal to the granite.

4. Sampling and analytical methods

Twelve biotite granite (15JKC-1–15JKC-12) and eleven fine-grained granite (15JKX-1–15JKX-11) fresh samples were collected from drill holes and mining tunnels for geochemical and isotopic analysis. The biotite granite and fine-grained granite are massive and equigranular (Fig. 7). The biotite granite is gray in color and composed of quartz

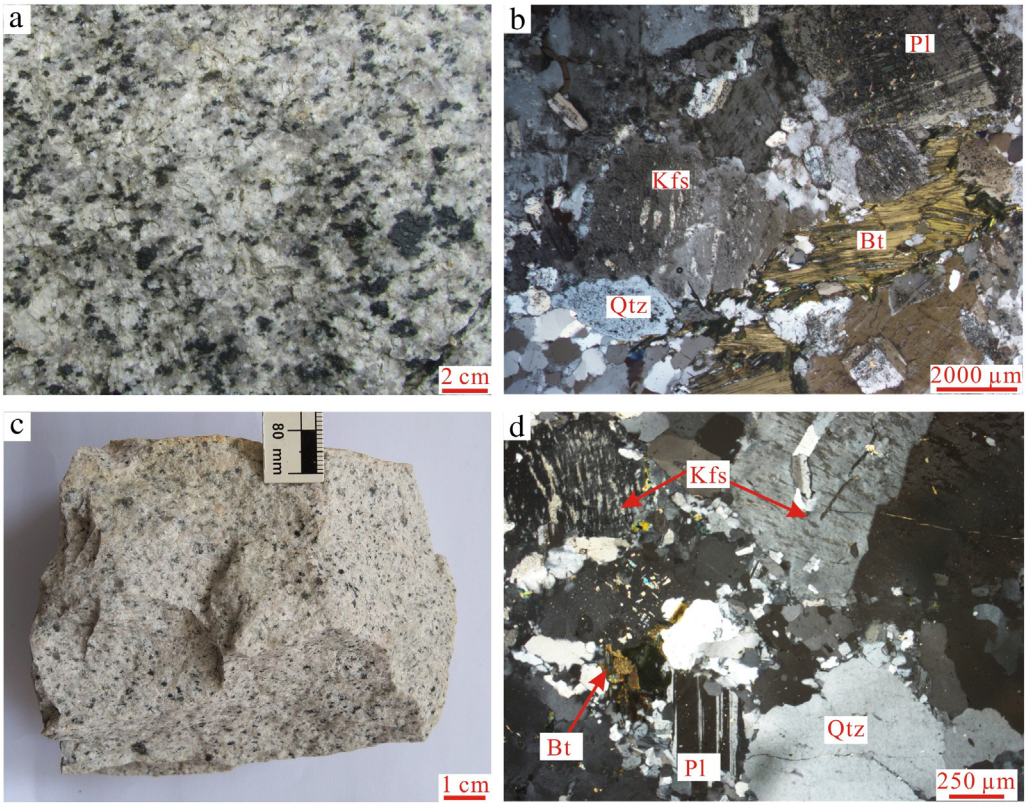

Fig. 7. Photograph (a), (c) and photomicrograph (b), (d) showing representative examples of the biotite granite and fine-grained granite associated with the Jinkeng deposit. Qtz = quartz, Kfs = K-feldspar, Pl = plagioclase, Bt = biotite.

(25–30 vol.%), K-feldspar (30–35 vol.%), plagioclase (20–25 vol.%), and biotite (5–10 vol.%) (Fig. 7b). The fine-grained granite is gray to light pink and contains quartz (30–35 vol.%), K-feldspar (30-35 vol.%), plagioclase (20–25 vol.%), and biotite (1–5 vol.%) (Fig. 7d). Eight molybdenite samples containing coexisting cassiterite and arsenopyrite that formed during the early stages of ore formation (Fig. 6b) were obtained from a mining tunnel for Re–Os isotopic analyses. Representative sampling locations are shown in Figs. 3 and 4.

4.1. Major and trace element analyses of whole rocks

Major and trace element concentrations were determined at the State Key Laboratory of Isotope Geochemistry, Guangzhou Institute of Geochemistry, Chinese Academy of Sciences (GIG-CAS), Guangzhou, China. Before analysis, rock samples were crushed into small chips and then ground to 200 mesh. Major element concentrations (wt.%) were determined on fused glasses made with a 1:8 ratio of sample to $Li_2B_4O_7$ flux, employing a Rigaku ZSX100e X-ray fluorescence (XRF) spectrometer. These XRF analyses have an accuracy of ca. 1% for SiO_2, ca. 5% for MnO and P_2O_5, and ca. 2% for other major elements (Li et al., 2003). Trace element concentrations, including the rare earth elements (REE), were determined using inductively coupled plasma–mass spectrometry (ICP–MS; Perkin-Elmer Sciex ELAN 6000) at GIG-CAS, following the procedures outlined by Li et al. (2002). Prior to analysis, powdered samples (50 mg) were digested with a mixed HNO_3 + HF acid attack in steel-bomb coated Teflon beakers for two days to ensure complete dissolution of refractory minerals. A Rh internal standard solution was used to monitor signal drift during analysis, and USGS rock standards G-2, W-2, MRG-1, and AGV-1, and Chinese rock standards GSD-12, GSR-1, GSR-2, and GSR-3 were used to calibrate elemental concentrations within the measured samples. Analytical precision is generally better than 5% (Li et al., 2002).

4.2. Mineral chemistry of biotite

The mineral chemistry analyses were obtained from polished thin sections of biotite using electron probe micro-analysis (EPMA) technique (i.e., JEOL JXA-8100 Superprobe) at the State Key Laboratory of Isotope Geochemistry, GIG-CAS. The operating conditions are as the following: 15 kV accelerating voltage, 20 nA beam current, 1 μm beam diameter, and ZAF correction procedure for data reduction. The detection limits for all elements are lower than 300 ppm, depending on the element concentrations. The following natural and synthetic standards were used: hornblende (Si, Na, Mg, Al, Ca, Ti), fluorite (F), barium chlorapatite (Cl), fayalite (Fe, Mn), K-feldspars (K), pure Sn metal (Sn). Chemical formulae of biotite were calculated based on 22 oxygen anions, and Fe^{2+} and Fe^{3+} was calculated after the method by Lin and Peng (1994).

4.3. Zircon LA–ICP–MS analysis

Zircons were separated from the biotite granite (14JKC-3) and fine-grained granite (sample 14JKX-4) using standard heavy liquid and magnetic techniques, followed by hand picking under a binocular microscope. About 100 zircons were randomly selected for mounting on adhesive tape prior to enclosure in epoxy resin and polishing to about half thickness. These zircons were then photographed under reflected and transmitted light, and imaged using the Zeiss Supra 55 field emission SEM equipped with a MonoCL4 cathodoluminescence detector at GIG-CAS to examine zircon textures and to select target sites for U–Pb isotopic analysis. Zircon U–Pb dating was carried out with an Agilent 7900a ICP–MS instrument coupled with a 193 nm wave laser microprobe at the CAS Key Laboratory of Mineralogy and Metallogeny, GIG-CAS. This analysis used a laser energy density of 4 J/cm^2 and a frequency of 10 Hz with an ablation spot of 31 μm in diameter and a 40 s ablation

Table 1
Major (wt.%) and trace element (ppm) compositions of the Jinkeng granites.

Samples	14JKC-1	14JKC-2	14JKC-3	14JKC-4	14JKC-5	14JKC-6	14JKC-7	14JKC-8	14JKC-9	14JKC-10	14JKC-11	14JKC-12	14JKX-1	14JKX-2	14JKX-3	14JKX-4	14JKX-5	14JKX-6	14JKX-7	14JKX-8	14JKX-9	14JKX-10	14JKX-11
Lithology	Biotite granite												Fine-grained granite										
SiO_2	75.5	75.1	74.6	75.2	74.6	75.2	75.2	74.7	75.9	74.7	75.0	75.0	75.4	75.9	75.4	76.3	75.9	75.7	75.9	76.1	76.1	76.7	76.0
Al_2O_3	12.5	12.6	12.8	12.8	12.7	12.6	12.7	12.6	12.6	12.7	13.0	13.2	12.6	12.4	12.5	12.3	12.5	12.4	12.5	12.5	12.6	12.5	12.5
TiO_2	0.07	0.07	0.10	0.10	0.07	0.08	0.08	0.08	0.07	0.10	0.10	0.09	0.08	0.07	0.08	0.06	0.07	0.07	0.08	0.06	0.07	0.06	0.07
Fe_2O_3T	2.04	2.10	2.38	2.01	2.12	2.05	2.48	2.34	1.75	2.27	2.07	1.91	2.15	1.86	2.18	1.43	1.61	2.06	1.81	1.85	1.82	1.09	2.11
MnO	0.13	0.12	0.14	0.11	0.13	0.12	0.17	0.14	0.10	0.12	0.11	0.11	0.10	0.09	0.15	0.04	0.05	0.09	0.09	0.10	0.11	0.03	0.13
MgO	0.02	0.00	0.04	0.06	0.02	0.02	0.01	0.02	0.01	0.04	0.07	0.06	0.00	0.01	0.00	0.00	0.00	0.01	0.01	0.01	0.01	0.01	0.01
CaO	0.75	0.73	0.80	0.82	0.64	0.56	0.73	0.70	0.67	0.76	0.71	0.76	0.73	0.74	0.70	0.76	0.78	0.76	0.68	0.56	0.57	0.53	0.60
Na_2O	3.53	3.56	3.49	3.43	3.54	3.49	3.49	3.52	3.41	3.60	3.57	3.65	3.34	3.20	3.49	3.32	3.31	3.20	3.06	3.08	3.16	3.16	3.15
K_2O	4.76	4.75	4.85	5.07	5.05	5.01	4.89	4.80	5.02	4.75	5.05	5.05	5.03	4.99	4.98	4.98	4.94	5.01	5.24	5.21	5.00	5.11	4.92
P_2O_5	0.00	0.01	0.01	0.01	0.01	0.00	0.00	0.01	0.00	0.01	0.01	0.01	0.00	0.00	0.01	0.00	0.00	0.00	0.00	0.00	0.00	0.00	0.00
L.O.I	0.10	0.12	0.23	0.33	0.10	0.25	0.04	0.13	0.14	0.17	0.26	0.28	0.22	0.41	0.13	0.39	0.47	0.29	0.32	0.11	0.18	0.43	0.08
Total	99.32	99.04	99.16	99.56	98.88	99.08	99.74	98.86	99.48	99.05	99.69	99.75	99.63	99.63	99.64	99.63	99.62	99.63	99.63	99.62	99.62	99.62	99.62
A/CNK	1.01	1.02	1.02	1.01	1.02	1.03	1.02	1.02	1.03	1.02	1.03	1.02	1.03	1.03	1.01	1.01	1.02	1.03	1.05	1.07	1.08	1.07	1.08
A/NK	1.14	1.15	1.16	1.15	1.12	1.12	1.15	1.14	1.14	1.15	1.15	1.15	1.15	1.16	1.12	1.13	1.15	1.16	1.17	1.17	1.19	1.17	1.19
TA	8.29	8.31	8.34	8.50	8.59	8.50	8.38	8.32	8.43	8.35	8.62	8.70	8.37	8.19	8.47	8.30	8.26	8.21	8.30	8.29	8.16	8.27	8.07
K_2O/N_2O	1.3	1.3	1.4	1.5	1.4	1.4	1.4	1.4	1.5	1.3	1.4	1.4	1.5	1.6	1.4	1.5	1.5	1.6	1.7	1.7	1.6	1.6	1.6
Sn	18.1	9.32	9.72	8.06	9.56	8.42	8.23	11.2	12.3	9.36	15.6	13.8	26.1	10.3	8.72	8.51	8.65	13.6	30.0	8.32	9.63	11.2	16.3
F	1160	880	1260	1630	1000	970	1040	1250	1080	1750	1550	860	660	2520	1860	2050	1470	1840	330	1330	700	1200	2150
Sc	7.81	7.78	6.30	6.35	6.13	6.09	6.30	6.32	6.48	6.44	5.98	6.06	4.88	6.57	10.4	7.98	7.25	7.35	6.94	7.55	7.72	6.18	4.48
Ti	409	403	542	552	418	418	437	463	431	566	514	506	409	414	408	402	405	397	392	410	398	373	393
V	3.20	3.22	4.38	2.91	3.08	3.32	4.39	3.58	3.74	4.22	4.63	6.52	2.18	1.32	3.74	1.34	1.21	3.95	2.93	1.91	2.12	2.52	2.53
Cr	9.51	16.2	216	40.6	16.6	21.1	22.8	20.7	5.16	24.5	17.4	13.9	18.7	18.9	23.1	31.5	22.7	12.6	24.2	22.3	8.07	14.1	12.1
Mn	883	862	1044	746	925	886	1180	1013	689	844	753	853	265	314	641	746	671	1097	626	694	797	184	981
Co	0.87	0.93	4.84	1.27	0.96	0.98	1.25	1.16	0.74	1.23	1.02	1.03	0.47	0.50	0.61	0.97	0.75	1.12	1.96	0.76	0.92	0.40	1.16
Ni	1.88	1.82	138	23.1	2.71	3.75	2.69	2.36	1.12	9.48	1.63	2.00	0.96	0.85	1.59	2.11	1.88	2.29	1.72	2.35	2.18	0.70	2.81
Cu	5.34	4.81	17.43	9.61	4.63	4.89	6.26	5.11	3.85	4.51	3.70	4.52	26.7	9.14	23.8	20.0	9.04	17.8	48.7	17.1	35.6	79.5	22.6
Zn	60.7	58.5	63.9	56.2	45.2	47.2	48.5	55.2	50.0	58.7	52.5	55.0	25.0	32.7	29.1	28.2	23.3	24.0	28.9	25.1	34.1	28.5	32.4
Ga	20.1	20.2	18.8	18.2	17.8	17.7	18.6	18.4	18.4	18.6	18.4	19.7	20.0	19.8	20.3	20.8	19.6	18.8	19.6	20.1	20.2	18.4	18.0
Ge	1.74	1.74	1.84	1.69	1.82	1.80	1.98	1.87	1.80	1.89	1.81	1.88	1.73	1.75	1.82	2.28	2.34	2.14	1.79	1.89	1.93	1.60	1.46
Rb	252	251	253	256	252	269	246	245	247	251	260	275	295	288	278	276	323	293	255	251	241	238	238
Sr	20.6	19.4	44.2	40.2	29.7	29.6	27.1	26.0	25.5	40.4	40.5	42.9	8.2	11.4	10.7	12.1	15.9	26.4	19.1	19.8	19.1	19.0	13.1
Zr	112	131	139	118	108	134	137	159	107	135	135	133	126	125	123	134	145	141	121	140	119	93	126

(continued on next page)

Table 1
Major (wt.%) and trace element (ppm) compositions of the Jinkeng granites.

Samples	14JKC-1	14JKC-2	14JKC-3	14JKC-4	14JKC-5	14JKC-6	14JKC-7	14JKC-8	14JKC-9	14JKC-10	14JKC-11	14JKC-12	14JKX-1	14JKX-2	14JKX-3	14JKX-4	14JKX-5	14JKX-6	14JKX-7	14JKX-8	14JKX-9	14JKX-10	14JKX-11
Nb	20.1	19.5	20.3	26.2	22.8	20.8	21.7	19.8	22.1	19.9	18.7	20.4	18.0	16.5	16.2	16.3	17.6	16.6	13.0	13.6	13.2	11.8	13.5
Cs	7.41	7.03	6.40	5.80	5.38	5.67	5.32	6.05	5.15	5.83	5.52	6.03	5.37	6.45	6.90	5.25	3.97	3.93	3.08	2.79	2.67	2.46	2.61
Ba	128	120	327	303	243	235	212	203	196	270	324	315	26.2	35.0	31.4	32.7	37.0	67.4	36.7	39.4	34.7	33.1	18.5
Hf	5.22	6.03	5.25	4.73	4.51	5.80	5.35	6.18	4.95	5.12	5.14	5.45	5.28	5.38	5.20	5.97	6.60	5.95	5.10	5.80	5.08	3.97	5.41
Ta	1.61	1.61	1.68	2.04	2.47	2.20	1.64	1.78	1.88	1.81	1.76	1.91	1.65	1.54	1.43	1.52	1.86	1.64	1.43	1.52	1.43	1.34	1.44
Pb	32.8	32.3	30.3	31.0	31.2	32.6	30.3	29.9	32.2	29.9	30.2	31.6	24.1	29.0	26.6	29.5	30.1	28.2	32.4	26.5	26.8	26.5	26.8
Th	17.3	22.6	23.1	23.0	19.8	25.5	23.9	15.0	22.9	16.4	23.6	24.1	26.0	22.1	21.0	24.4	25.2	21.7	19.5	20.3	21.4	19.0	12.3
U	7.12	5.93	3.98	6.55	3.96	4.18	5.70	5.07	5.19	8.09	6.38	6.77	4.10	6.64	6.18	7.27	6.16	5.69	4.40	4.90	5.40	4.20	5.52
La	21.1	24.0	33.6	32.2	30.8	26.8	26.5	29.7	30.9	32.2	28.9	31.2	7.07	19.3	13.6	24.6	19.8	26.3	16.5	21.2	22.6	18.2	8.52
Ce	47.2	53.6	67.5	66.7	63.8	56.2	59.0	63.1	62.2	66.4	60.8	65.1	20.0	45.1	34.2	58.8	46.4	62.7	39.9	50.6	52.7	43.0	20.9
Pr	6.36	7.12	8.48	8.01	7.73	6.99	7.11	7.85	8.03	8.15	7.48	7.73	3.06	6.18	4.90	8.04	6.37	8.43	5.51	6.54	6.90	5.67	2.77
Nd	25.6	28.5	31.7	29.5	28.6	26.4	27.2	29.2	29.8	30.3	28.6	29.3	11.9	25.3	19.9	32.6	26.0	33.2	22.1	26.1	27.6	22.7	11.6
Sm	7.35	8.36	7.93	7.58	7.16	6.73	6.75	6.91	7.08	7.70	7.53	7.06	3.71	6.91	5.67	9.30	7.62	8.79	5.88	7.00	7.36	5.96	3.35
Eu	0.24	0.24	0.49	0.48	0.39	0.39	0.31	0.33	0.35	0.44	0.46	0.43	0.07	0.13	0.11	0.14	0.14	0.22	0.12	0.14	0.15	0.11	0.07
Gd	7.44	8.63	8.26	8.16	7.06	6.63	6.53	6.63	6.59	7.62	7.59	6.73	4.40	7.18	5.70	9.74	7.94	8.14	5.60	7.14	7.36	5.51	3.50
Tb	1.38	1.61	1.54	1.61	1.29	1.24	1.19	1.14	1.15	1.34	1.34	1.19	0.81	1.22	1.02	1.68	1.39	1.33	0.96	1.24	1.25	0.92	0.56
Dy	8.50	9.78	9.55	10.1	7.98	7.63	7.25	6.93	6.89	8.00	7.97	7.16	5.67	8.31	6.89	11.31	9.31	8.65	6.32	8.33	8.21	5.93	3.66
Ho	1.80	2.03	2.00	2.18	1.70	1.64	1.55	1.48	1.46	1.62	1.61	1.44	1.19	1.73	1.41	2.31	1.93	1.74	1.29	1.74	1.67	1.16	0.72
Er	4.98	5.41	5.55	6.08	4.73	4.55	4.32	4.16	4.06	4.45	4.24	4.07	3.27	4.82	4.00	6.31	5.38	4.75	3.57	4.84	4.58	3.12	1.94
Tm	0.72	0.80	0.82	0.90	0.74	0.69	0.66	0.62	0.62	0.65	0.63	0.60	0.48	0.73	0.60	0.94	0.82	0.72	0.54	0.73	0.68	0.46	0.29
Yb	4.63	4.98	5.28	5.72	4.73	4.57	4.30	4.10	4.05	4.35	4.12	3.98	3.04	4.66	3.80	5.92	5.40	4.62	3.50	4.74	4.28	2.91	1.88
Lu	0.70	0.74	0.79	0.85	0.73	0.70	0.66	0.64	0.62	0.65	0.61	0.61	0.46	0.69	0.57	0.87	0.81	0.69	0.52	0.71	0.64	0.42	0.28
Y	48.3	32.2	38.3	39.2	45.0	50.3	42.7	42.2	25.2	42.1	40.4	36.1	26.3	44.1	32.6	56.4	51.2	42.9	30.2	45.9	44.4	26.2	15.0
ΣREE	138	156	183	180	167	151	153	163	164	174	162	167	65	132	102	173	139	170	112	141	146	116	60
LREE/HREE	3.6	3.6	4.4	4.1	4.8	4.5	4.8	5.3	5.4	5.1	4.8	5.5	2.4	3.5	3.3	3.4	3.2	4.6	4.0	3.8	4.1	4.7	3.7
$(La/Sm)_N$	1.9	1.8	2.7	2.7	2.8	2.6	2.5	2.8	2.8	2.7	2.5	2.9	1.2	1.8	1.5	1.7	1.7	1.9	1.8	2.0	2.0	2.0	1.6
$(Gd/Yb)_N$	1.3	1.4	1.3	1.2	1.2	1.2	1.3	1.3	1.3	1.4	1.5	1.4	1.2	1.3	1.2	1.4	1.2	1.5	1.3	1.2	1.4	1.6	1.5
$(La/Yb)_N$	3.3	3.5	4.6	4.0	4.7	4.2	4.4	5.2	5.5	5.3	5.0	5.6	1.7	3.0	2.6	3.0	2.6	4.1	3.4	3.2	3.8	4.5	3.3
δEu	0.10	0.09	0.18	0.18	0.16	0.18	0.14	0.15	0.15	0.17	0.18	0.19	0.05	0.06	0.06	0.05	0.06	0.08	0.06	0.06	0.06	0.06	0.06
Zr + Nb + Ce + Y	228	255	284	271	239	254	261	284	230	263	255	255	190	230	206	265	260	263	204	250	230	174	176
Rb/Sr	12	13	6	6	8	9	9	9	10	6	6	6	36	25	26	23	20	11	13	13	13	13	18
K/Rb	158	159	161	165	168	156	165	165	169	158	162	153	142	145	149	151	128	143	171	173	174	179	172
Nb/Ta	12	12	12	13	9	9	13	11	12	11	11	11	11	11	11	11	9	10	9	9	9	9	9
Zr/Hf	22	22	27	25	24	23	26	26	22	26	26	24	24	23	24	22	22	24	24	24	24	23	23
Th/U	4	4	6	4	6	6	4	5	4	4	4	4	3	3	3	3	3	4	4	4	4	5	2
Y + Nb	68.4	51.6	58.6	65.4	67.8	71.0	64.5	61.9	47.2	61.9	59.1	56.5	44.3	60.7	48.8	72.6	68.7	59.4	43.1	59.6	57.5	38.0	28.6
T_{Zr}(°C)	758	771	776	761	754	774	775	787	755	772	773	771	768	768	764	773	780	778	767	782	770	749	774

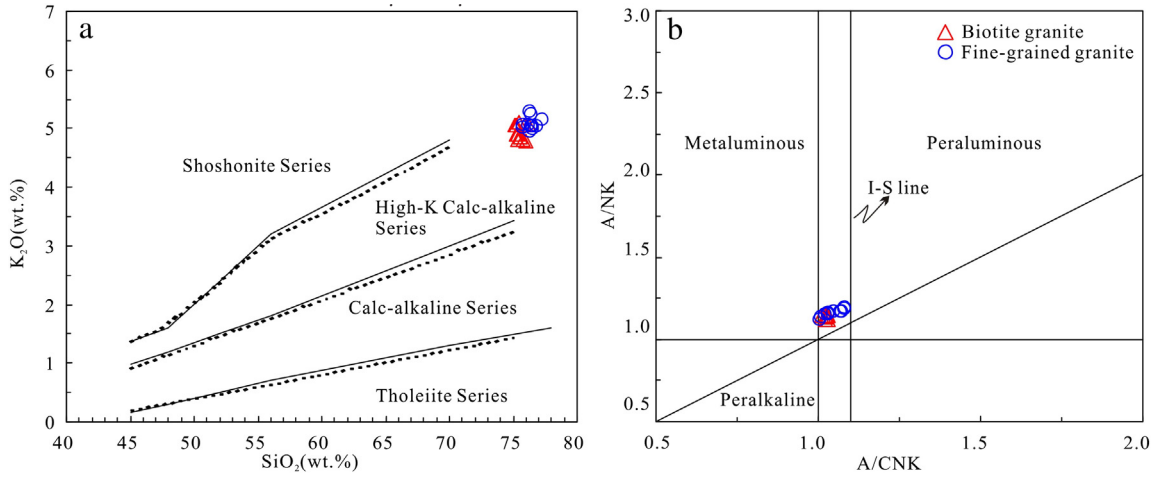

Fig. 8. (a) K_2O versus SiO_2 (Peccerillo and Taylor, 1976) and (b) A/NK versus A/CNK diagrams for the Jinkeng granites.

period. Corrections were made for mass bias drift as determined by reference to a NIST SRM 610 glass standard. A Temora standard zircon was used for age calibration ($^{206}Pb/^{238}U = 416.8$ Ma; Black et al., 2003) and the analytical procedures used were similar to those described by Li et al. (2011). Offline selection and integration of background and analyte signals, and time-drift correction and quantitative calibration for U–Pb dating were undertaken using ICPMS DataCal 8.4 software (Liu et al., 2010). Common Pb was corrected following Andersen (2002), and the results and associated age calculations are shown in a concordia diagram constructed using ISOPLOT (V.3.0; Ludwig, 2003).

4.4. Zircon Hf isotope analysis

In situ zircon Lu–Hf isotopic analysis was undertaken using a Neptune Plus multi-collector ICP–MS equipped with a RESOlution M-50 LA system at the State Key Laboratory of Isotope Geochemistry, GIGCAS. Lu–Hf isotopic measurements were made on the same spots previously used for U–Pb analysis using a spot size of 45 μm, a repetition rate of 8 Hz, and a laser energy of 80 mJ. Helium was used as a carrier gas and a small amount of nitrogen was added to the gas line to enhance sample signals. A normal single spot analysis consists of 30 s gas blank collection and 30 s laser ablation periods using an integration time of 0.131 s, yielding about 200 cycles of data. The isobaric interference of ^{176}Yb and ^{176}Lu on ^{176}Hf was corrected using ^{173}Yb and ^{175}Lu concentrations, and $^{176}Hf/^{177}Hf$ ratios were normalized to a $^{179}Hf/^{177}Hf$ value of 0.7325 using an exponential law for mass bias correction. A Penglai standard zircon was used as a reference standard (Li et al., 2010) and the analytical procedures were identical to those described by Wu et al. (2006). Initial Hf isotope ratios are presented as $\varepsilon_{Hf}(t)$ values that were calculated using the Chondritic Uniform Reservoir (CHUR) value at the time of zircon crystallization and present-day $^{176}Hf/^{177}Hf$ and $^{176}Lu/^{177}Hf$ ratios of chondrite and depleted mantle, respectively (Blichert-Toft and Albarede, 1997). Initial $^{176}Hf/^{177}Hf$ values were calculated based on a ^{176}Lu decay constant of 1.867×10^{-11}/a (Söderlund et al., 2004), and single-stage model Hf ages (T_{DM1}) were determined with reference to the depleted mantle using a present-day $^{176}Lu/^{177}Hf$ ratio of 0.28325 and a $^{176}Lu/^{177}Hf$ ratio of 0.0384 (Griffin et al., 2000). Two-stage model Hf ages (T_{DM2}) were computed using a $^{176}Lu/^{177}Hf$ value of 0.015 for the average continental crust (Griffin et al., 2002). Analysis of the Penglai standard zircon yielded $^{176}Hf/^{177}Hf$ and $^{176}Lu/^{177}Hf$ ratios of 0.282907 ± 0.000016 (2σ, $n = 20$) and 0.000303, respectively, consistent with the recommended $^{176}Hf/^{177}Hf$ values for this standard (0.282906 ± 0.000016, 2σ, $n = 117$; Li et al., 2010).

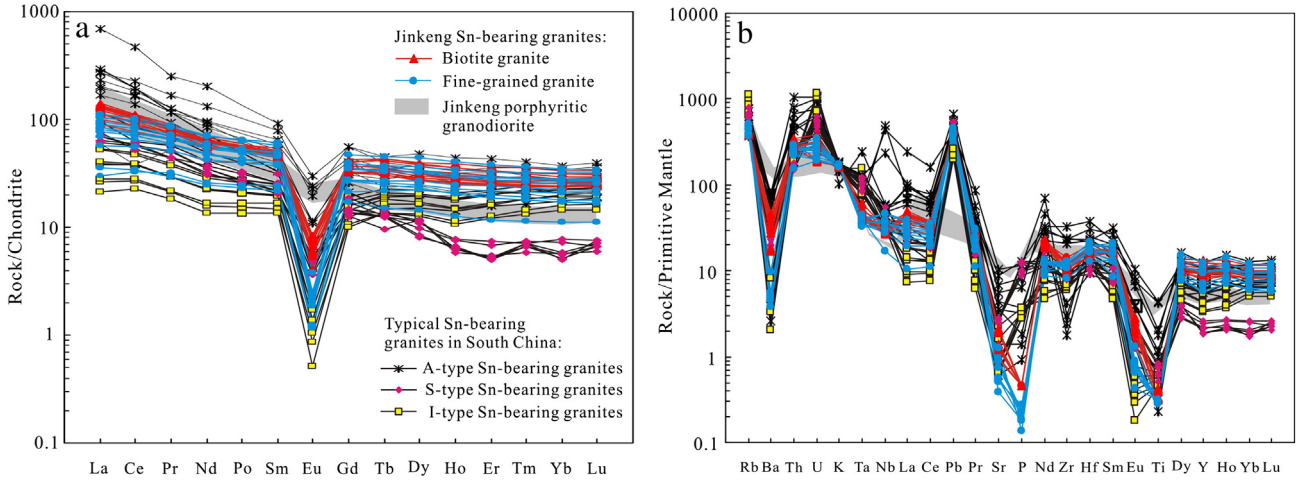

Fig. 9. Chondrite-normalized REE (a) and primitive-mantle-normalized multi-element (b) diagrams for samples of the biotite granite and fine-grained granite associated with the Jinkeng deposit of eastern Guangdong Province (normalizing values are from Sun and McDonough, 1989). Data of A-type, S-type and highly fractionated I-type Sn-bearing granites in South China for comparison are from Wang et al. (2013), Feng et al. (2012) and Xu et al. (2016), respectively. Data of the porphyritic granodiorite in Jinkeng deposit for comparison are from authors' unpublished data.

Table 2
Elecrton-microprobe results of biotite from the Jinkeng granites and porphyritic granodiorite.

Sample	Biotite granite					Fine-grained granite								Porphyritic granodiorite							
	15JKC-1			15JKC-3		15JKX-1			15JKX-3			15JKX-5		15JKSC-1			15JKSC-3				
	1	2	3	1	2	1	2	3	1	2	3	1	2	1	2	3	1	2	3	4	5
SiO_2	34.22	35.14	34.62	35.04	34.21	34.36	33.50	34.33	34.43	34.09	34.07	33.07	32.96	36.40	36.50	36.44	36.67	36.60	36.89	36.71	36.56
TiO_2	2.34	2.74	2.52	2.65	2.31	2.22	2.58	1.27	2.87	2.28	1.32	1.28	1.25	1.86	1.80	1.83	1.64	1.77	1.92	2.00	1.66
Al_2O_3	17.53	18.17	17.86	18.13	17.56	18.16	17.54	19.24	18.31	18.20	18.62	18.74	18.67	15.78	16.27	15.83	16.06	16.13	16.25	15.64	15.73
FeO^T	32.00	29.39	31.50	29.19	31.90	30.68	31.48	31.29	30.60	31.21	31.27	32.28	32.16	21.97	21.75	22.63	22.59	23.17	22.24	23.01	22.86
MnO	0.09	0.20	0.10	0.22	0.08	0.10	0.06	0.11	0.06	0.08	0.13	0.11	0.14	0.11	0.08	0.08	0.07	0.08	0.10	0.12	0.06
MgO	0.89	0.92	0.97	0.94	0.87	0.44	0.33	0.23	0.42	0.17	0.15	0.16	0.15	8.62	8.70	8.20	8.38	8.20	8.64	8.79	8.75
CaO	0.01	0.00	0.00	0.00	0.00	0.00	0.06	0.00	0.00	0.00	0.00	0.01	0.00	0.05	0.00	0.00	0.03	0.00	0.00	0.00	0.02
Na_2O	0.10	0.08	0.11	0.11	0.09	0.05	0.05	0.07	0.10	0.11	0.03	0.01	0.07	0.18	0.05	0.00	0.20	0.09	0.07	0.06	0.04
K_2O	9.16	9.37	9.46	9.42	9.26	9.28	8.47	9.41	9.34	9.37	9.22	8.72	8.84	9.56	9.48	9.71	9.40	9.62	9.73	9.55	9.49
F	0.32	0.22	0.20	0.25	0.28	0.54	0.22	0.22	0.26	0.25	0.29	0.21	0.18	0.00	0.00	0.04	0.00	0.02	0.00	0.04	0.00
Cl	0.01	0.02	0.07	0.04	0.03	0.09	0.08	0.06	0.10	0.03	0.03	0.03	0.03	0.07	0.07	0.07	0.07	0.07	0.06	0.07	0.06
SnO_2	0.01	0.00	0.00	0.00	0.00	0.01	0.00	0.00	0.00	0.00	0.01	0.00	0.00	0.00	0.00	0.00	0.00	0.00	0.00	0.00	0.00
Total	96.53	96.16	94.45	97.50	96.08	95.67	94.24	96.11	96.36	95.68	95.01	94.53	94.35	94.22	94.32	94.53	94.75	95.53	95.56	95.65	94.98
Fe_2O_3 (calc.)[a]	2.69	3.01	2.72	2.96	2.66	2.89	2.99	2.72	2.96	2.79	2.75	2.66	2.54	3.43	3.69	3.60	3.60	3.56	3.65	3.53	3.48
FeO (calc.)[a]	29.58	26.68	29.05	26.52	29.51	28.09	28.79	28.84	27.94	28.69	28.79	29.89	29.87	18.89	18.43	19.39	19.36	19.97	18.96	19.84	19.73
Cations based on 22 oxygen anions																					
Si^{4+}	5.435	5.517	5.443	5.519	5.439	5.523	5.431	5.450	5.437	5.447	5.477	5.373	5.373	5.622	5.607	5.628	5.632	5.605	5.612	5.606	5.622
Al^{IV}	2.565	2.483	2.557	2.481	2.561	2.477	2.569	2.550	2.563	2.553	2.523	2.627	2.627	2.378	2.393	2.372	2.368	2.395	2.388	2.394	2.378
T-site	8.000	8.000	8.000	8.000	8.000	8.000	8.000	8.000	8.000	8.000	8.000	8.000	8.000	8.000	8.000	8.000	8.000	8.000	8.000	8.000	8.000
Al^{VI}	0.717	0.879	0.753	0.884	0.731	0.963	0.783	1.051	0.844	0.875	1.004	0.962	0.961	0.495	0.554	0.510	0.539	0.516	0.526	0.421	0.472
Ti^{4+}	0.280	0.324	0.298	0.314	0.277	0.268	0.315	0.151	0.340	0.274	0.160	0.157	0.153	0.216	0.208	0.212	0.190	0.204	0.219	0.230	0.192
Fe^{3+}	0.321	0.356	0.322	0.351	0.318	0.349	0.365	0.325	0.351	0.336	0.333	0.325	0.312	0.399	0.427	0.418	0.416	0.411	0.417	0.405	0.402
Fe^{2+}	3.929	3.502	3.820	3.494	3.924	3.775	3.904	3.830	3.689	3.834	3.870	4.061	4.072	2.440	2.368	2.505	2.487	2.557	2.413	2.534	2.538
Mn^{2+}	0.013	0.027	0.014	0.030	0.011	0.014	0.008	0.015	0.009	0.011	0.018	0.015	0.019	0.014	0.011	0.010	0.009	0.010	0.012	0.016	0.008
Mg^{2+}	0.210	0.216	0.227	0.221	0.206	0.105	0.080	0.055	0.098	0.040	0.036	0.039	0.037	1.985	1.993	1.889	1.918	1.873	1.959	2.001	2.006
O-site	5.470	5.304	5.433	5.293	5.466	5.474	5.454	5.426	5.332	5.371	5.421	5.559	5.555	5.548	5.561	5.544	5.559	5.571	5.547	5.606	5.618
Ca^{2+}	0.002	0.000	0.000	0.000	0.000	0.000	0.010	0.000	0.001	0.000	0.000	0.002	0.000	0.008	0.000	0.000	0.006	0.000	0.000	0.000	0.003
Na^+	0.029	0.023	0.034	0.033	0.028	0.014	0.014	0.022	0.031	0.034	0.010	0.003	0.021	0.052	0.014	0.001	0.059	0.027	0.020	0.017	0.013
K^+	1.856	1.876	1.897	1.892	1.878	1.902	1.753	1.905	1.881	1.909	1.890	1.808	1.839	1.885	1.858	1.913	1.842	1.880	1.889	1.860	1.861
Interlayer	1.887	1.900	1.931	1.925	1.906	1.916	1.777	1.927	1.913	1.944	1.900	1.814	1.860	1.945	1.872	1.914	1.907	1.908	1.909	1.877	1.877
F	0.162	0.109	0.101	0.125	0.142	0.276	0.111	0.108	0.128	0.128	0.146	0.109	0.092	0.000	0.000	0.018	0.000	0.010	0.000	0.021	0.000
Cl	0.003	0.006	0.019	0.011	0.009	0.026	0.021	0.015	0.026	0.008	0.008	0.007	0.007	0.018	0.018	0.019	0.018	0.019	0.017	0.017	0.016
OH	3.834	3.885	3.880	3.865	3.849	3.699	3.868	3.877	3.846	3.864	3.846	3.884	3.901	3.982	3.982	3.964	3.982	3.971	3.983	3.962	3.984
Fe/(Fe + Mg)	0.953	0.947	0.948	0.946	0.954	0.975	0.982	0.987	0.976	0.990	0.992	0.991	0.992	0.588	0.584	0.607	0.602	0.613	0.591	0.595	0.594
$Fe^{3+}/(Fe^{2+} + Fe^{3+})$	0.076	0.092	0.078	0.091	0.075	0.085	0.086	0.078	0.087	0.081	0.079	0.074	0.071	0.140	0.153	0.143	0.143	0.138	0.147	0.138	0.137

[a] Using surplus oxygen method (Lin and Peng, 1994) to allocate the iron.

4.5. Molybdenite Re–Os dating

Eight molybdenite samples from the Jinkeng Sn plymetallic deposit were crushed, separated, and sieved to obtain monomineralic molybdenite separates with purity > 99%. The dissolution of molybdenite, purification and separation of Re–Os, and analysis of Re–Os contents in molybdenite were undertaken at the Key Laboratory of Isotope Geochemistry, GIG-CAS. Re and Os concentrations and isotopic compositions were determined with a Thermo Scientific X series 2 ICP–MS using the chemical separation processes and analytical methods described by Sun et al. (2010). Uncertainties in spike calibrations, weighing of both spikes and samples, mass spectrometry measurement of isotope ratios, mass

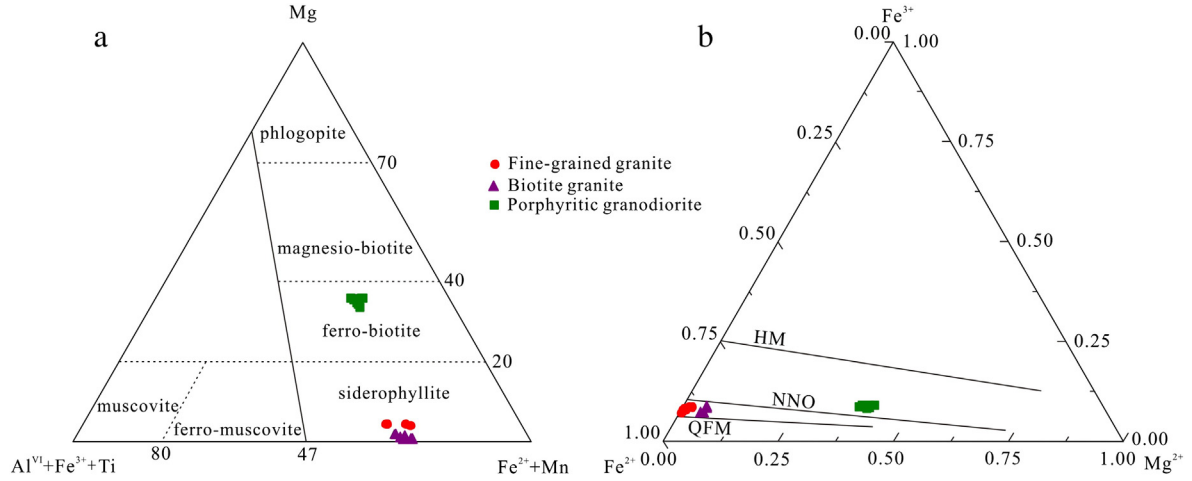

Fig. 10. (a) Classification of biotite from the Jinkeng granites and porphyritic granodiorite (Foster, 1960). (b) Diagram of Fe^{3+}–Fe^{2+}–Mg for biotite from the Jinkeng granites and porphyritic granodiorite (Wones and Eugster, 1965).

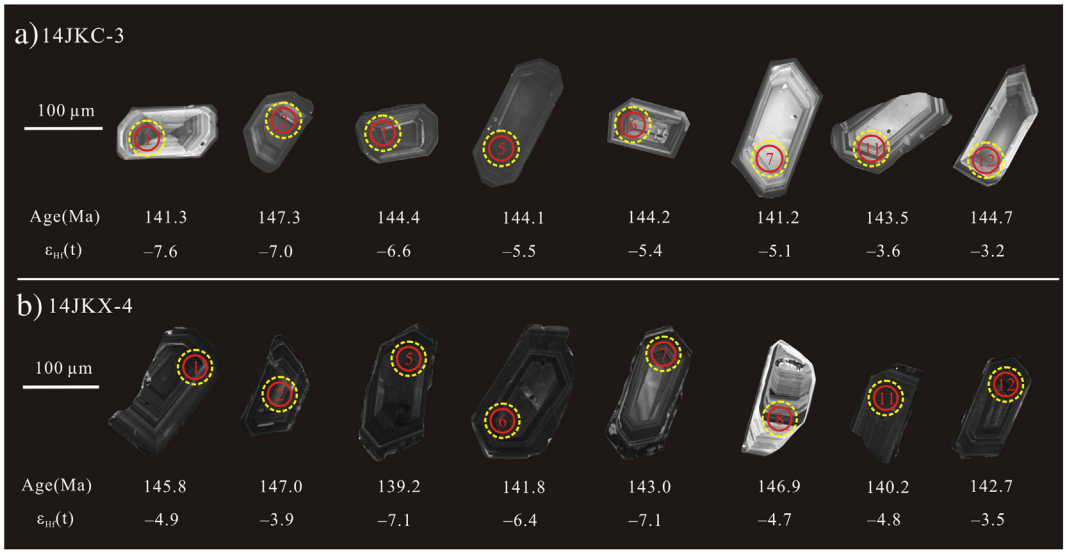

Fig. 11. Representative cathodoluminescence (CL) images of zircons from the Jinkeng biotite granite (a) and fine-grained granite (b) in eastern Guangdong; numbers indicate analysis numbers, U–Pb ages, and $\varepsilon_{Hf}(t)$ values, where U–Pb analysis spots are shown as solid circles and Hf isotope spots are shown as dashed circles.

Table 3
Zircon LA–ICP–MS U–Pb ages data for the Jinkeng granites.

Spot no.	Pb (ppm)	Th (ppm)	U (ppm)	Th/U	$^{207}Pb/^{206}Pb$	1σ	$^{207}Pb/^{235}U$	1σ	$^{206}Pb/^{238}U$	1σ	$^{207}Pb/^{235}U$	1σ	$^{206}Pb/^{238}U$	1σ
Sample 14JKC-3: biotite granite (excluding spot 14JKC-3-4, 14JKC-3-10, 14JKC-3-24, 14JKC-3-30)														
14JKC-3-1	34	1101	1138	1.0	0.04780	0.00131	0.14693	0.00410	0.02215	0.00029	139.2	3.6	141.3	1.8
14JKC-3-2	16	397	531	0.7	0.04961	0.00166	0.15752	0.00484	0.02311	0.00039	148.5	4.2	147.3	2.5
14JKC-3-3	104	4110	3046	1.3	0.04735	0.00104	0.14857	0.00339	0.02265	0.00032	140.6	3.0	144.4	2.0
14JKC-3-5	86	3432	2547	1.3	0.04762	0.00120	0.14931	0.00384	0.02261	0.00029	141.3	3.4	144.1	1.8
14JKC-3-6	28	678	930	0.7	0.04855	0.00149	0.15214	0.00503	0.02263	0.00039	143.8	4.4	144.2	2.5
14JKC-3-7	20	541	640	0.8	0.04932	0.00212	0.14961	0.00568	0.02214	0.00036	141.6	5.0	141.2	2.3
14JKC-3-8	60	2574	1748	1.5	0.04913	0.00192	0.14792	0.00410	0.02216	0.00042	140.1	3.6	141.3	2.7
14JKC-3-9	58	2058	1729	1.2	0.04919	0.00109	0.15443	0.00366	0.02270	0.00030	145.8	3.2	144.7	1.9
14JKC-3-11	21	588	670	0.9	0.04845	0.00116	0.15034	0.00396	0.02251	0.00031	142.2	3.5	143.5	2.0
14JKC-3-12	35	1285	1025	1.3	0.05043	0.00119	0.15802	0.00425	0.02270	0.00028	149.0	3.7	144.7	1.8
14JKC-3-13	21	846	588	1.4	0.04754	0.00158	0.15012	0.00496	0.02300	0.00026	142.0	4.4	146.6	1.7
14JKC-3-14	17	530	556	1.0	0.04810	0.00279	0.14541	0.00722	0.02231	0.00036	137.9	6.4	142.2	2.3
14JKC-3-15	42	1772	1214	1.5	0.04645	0.00118	0.14516	0.00413	0.02268	0.00027	137.6	3.7	144.5	1.7
14JKC-3-16	27	873	871	1.0	0.05032	0.00157	0.15701	0.00560	0.02262	0.00035	148.1	4.9	144.2	2.2
14JKC-3-17	21	880	632	1.4	0.04632	0.00158	0.14740	0.00562	0.02298	0.00030	139.6	5.0	146.5	1.9
14JKC-3-18	98	2960	3261	0.9	0.04637	0.00093	0.14496	0.00334	0.02266	0.00030	137.5	3.0	144.4	1.9
14JKC-3-19	81	2757	2540	1.1	0.04777	0.00157	0.14636	0.00383	0.02260	0.00044	138.7	3.4	144.1	2.7
14JKC-3-20	121	4392	3816	1.2	0.04608	0.00094	0.14395	0.00319	0.02259	0.00029	136.6	2.8	144.0	1.8
14JKC-3-21	15	362	512	0.7	0.04964	0.00171	0.16044	0.00509	0.02360	0.00043	151.1	4.5	150.3	2.7
14JKC-3-22	58	1738	1903	0.9	0.04924	0.00108	0.15420	0.00364	0.02263	0.00029	145.6	3.2	144.2	1.9
14JKC-3-23	48	1158	1667	0.7	0.05183	0.00383	0.15264	0.00443	0.02252	0.00042	144.2	3.9	143.6	2.7
14JKC-3-25	53	1615	1746	0.9	0.04852	0.00126	0.15202	0.00405	0.02268	0.00033	143.7	3.6	144.6	2.1
14JKC-3-26	38	1249	1220	1.0	0.04932	0.00159	0.15870	0.00503	0.02342	0.00041	149.6	4.4	149.3	2.6
14JKC-3-27	35	1072	1136	0.9	0.04944	0.00132	0.15483	0.00428	0.02271	0.00029	146.2	3.8	144.8	1.9
14JKC-3-28	28	649	931	0.7	0.05079	0.00159	0.16162	0.00479	0.02324	0.00034	152.1	4.2	148.1	2.1
14JKC-3-29	7	221	234	0.9	0.04941	0.00241	0.15556	0.00735	0.02309	0.00034	146.8	6.5	147.1	2.2
Sample 14JKX-4: fine-grained granite														
14JKX-4-1	127	2027	4101	0.5	0.04927	0.00159	0.15657	0.00492	0.02288	0.00031	147.7	4.3	145.8	2.0
14JKX-4-2	69	1046	2214	0.5	0.04862	0.00160	0.15716	0.00537	0.02306	0.00029	148.2	4.7	147.0	1.8
14JKX-4-3	108	1490	3669	0.4	0.05215	0.00160	0.16271	0.00512	0.02236	0.00024	153.1	4.5	142.5	1.5
14JKX-4-4	109	1992	3842	0.5	0.04969	0.00138	0.15231	0.00418	0.02199	0.00024	144.0	3.7	140.2	1.5
14JKX-4-5	124	2036	4340	0.5	0.04834	0.00144	0.14742	0.00433	0.02183	0.00021	139.6	3.8	139.2	1.3
14JKX-4-6	68	821	2298	0.4	0.05100	0.00191	0.15763	0.00576	0.02225	0.00031	148.6	5.1	141.8	1.9
14JKX-4-7	63	1603	1902	0.8	0.05001	0.00181	0.15684	0.00604	0.02243	0.00034	147.9	5.3	143.0	2.2
14JKX-4-8	51	513	1589	0.3	0.04839	0.00231	0.15624	0.00775	0.02304	0.00047	147.4	6.8	146.9	2.9
14JKX-4-9	140	1807	4389	0.4	0.04836	0.00133	0.15090	0.00436	0.02240	0.00030	142.7	3.8	142.8	1.9
14JKX-4-10	121	1652	4095	0.4	0.04886	0.00125	0.15120	0.00377	0.02228	0.00021	143.0	3.3	142.0	1.3
14JKX-4-11	136	2181	4603	0.5	0.04953	0.00146	0.15210	0.00464	0.02199	0.00020	143.8	4.1	140.2	1.2
14JKX-4-12	119	1698	3868	0.4	0.04989	0.00130	0.15572	0.00415	0.02238	0.00024	146.9	3.6	142.7	1.5
14JKX-4-13	174	2666	5451	0.5	0.04972	0.00131	0.15534	0.00431	0.02243	0.00029	146.6	3.8	143.0	1.8
14JKX-4-14	79	1205	2386	0.5	0.05088	0.00160	0.15968	0.00537	0.02246	0.00031	150.4	4.7	143.2	2.0
14JKX-4-15	128	1594	4397	0.4	0.05142	0.00119	0.15708	0.00362	0.02198	0.00018	148.1	3.2	140.2	1.2
14JKX-4-16	133	1475	4448	0.3	0.05096	0.00131	0.15561	0.00420	0.02195	0.00024	146.9	3.7	140.0	1.5
14JKX-4-17	155	2598	4851	0.5	0.04994	0.00127	0.14733	0.00420	0.02119	0.00031	139.6	3.7	135.2	2.0
14JKX-4-18	178	3148	5668	0.6	0.05092	0.00133	0.15096	0.00446	0.02125	0.00030	142.8	3.9	135.5	1.9
14JKX-4-19	127	1690	4116	0.4	0.05046	0.00147	0.15070	0.00471	0.02150	0.00035	142.5	4.2	137.1	2.2

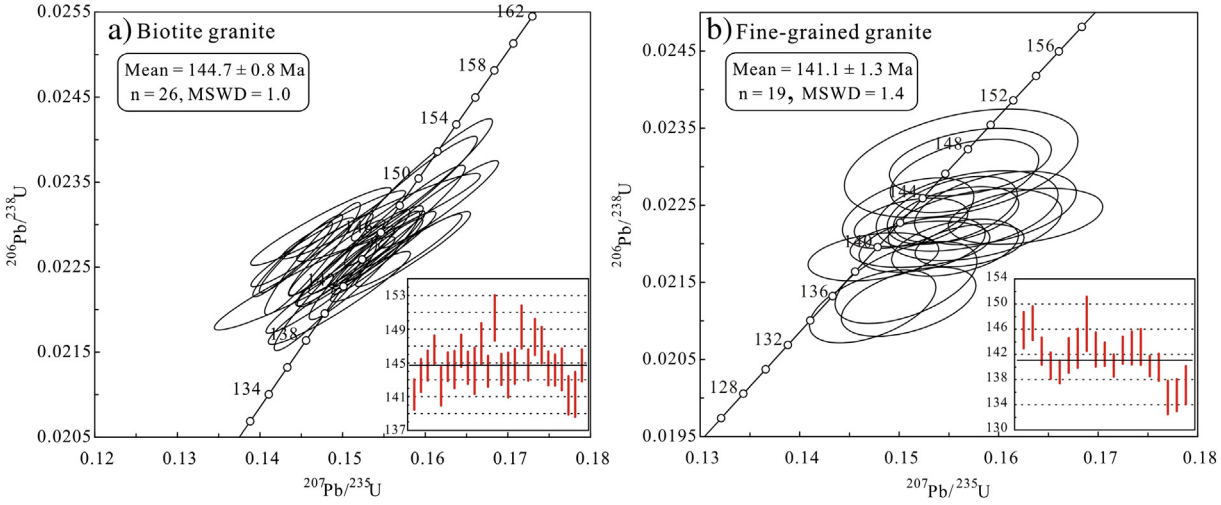

Fig. 12. Zircon U–Pb concordia diagrams and weighted mean age calculation for the Jinkeng biotite granite (a) and fine-grained granite (b).

fractionation factors, and the decay constant of ^{187}Re were considered during these analyses (Sun et al., 2010).

5. Analytical results

5.1. Whole-rock major and trace elements

The whole-rock geochemical compositions of biotite and fine-grained granite from the Jinkeng deposit are listed in Table 1. The granites are compositionally similar to each other, and are characterized by high SiO_2 (74.6–76.7 wt.%, mean = 75.5 wt.%), and low Al_2O_3 (12.3–13.2 wt.%, mean = 12.6 wt.%), Fe_2O_3T (1.09–2.48 wt.%), P_2O_5 (≤0.01 wt.%), TiO_2 (0.07–0.10 wt.%), MgO (0.00–0.07 wt.%), and CaO (0.53–0.82 wt.%). Total alkalis (8.07–8.70 wt.%, mean = 8.36 wt.%) and K_2O/Na_2O values (1.3–1.7, mean = 1.5) are high, characteristic of high-K, calc-alkaline rocks (Fig. 8a). They are weakly peraluminous, with alumina saturation index (ASI) values (A/CNK, molar $Al_2O_3/[CaO + K_2O + Na_2O]$) of 1.01–1.08 (Fig. 8b).

Table 4
Zircon Lu–Hf isotopic compositions of the Jinkeng granites.

Spot no.	Age (Ma)	$^{176}Yb/^{177}Hf$	$^{176}Lu/^{177}Hf$	$^{176}Hf/^{177}Hf$	1σ	$^{176}Hf/^{177}Hf_i$	$\varepsilon_{Hf}(0)$	$\varepsilon_{Hf}(t)$	1σ	t_{DM1} (Ma)	t_{DM2} (Ma)	$f_{Lu/Hf}$
Sample 14JKC-3 biotite granite												
14JKC-3-1	145	0.064358	0.002090	0.282538	0.000010	0.282532	−8.3	−5.3	0.4	1040	1534	−0.94
14JKC-3-2	145	0.071949	0.002175	0.282595	0.000010	0.282589	−6.3	−3.3	0.3	960	1406	−0.93
14JKC-3-3	145	0.142988	0.004195	0.282497	0.000012	0.282486	−9.7	−6.9	0.4	1166	1638	−0.87
14JKC-3-5	145	0.134344	0.004069	0.282538	0.000012	0.282527	−8.3	−5.5	0.4	1100	1545	−0.88
14JKC-3-6	145	0.130338	0.004031	0.282506	0.000012	0.282495	−9.4	−6.6	0.4	1148	1618	−0.88
14JKC-3-7	145	0.066384	0.002040	0.282547	0.000010	0.282542	−7.9	−5.0	0.3	1025	1513	−0.94
14JKC-3-8	145	0.066854	0.002076	0.282589	0.000009	0.282584	−6.5	−3.5	0.3	966	1419	−0.94
14JKC-3-9	145	0.091109	0.002680	0.282546	0.000011	0.282538	−8.0	−5.1	0.4	1046	1521	−0.92
14JKC-3-11	145	0.095681	0.002924	0.282475	0.000009	0.282467	−10.5	−7.6	0.3	1157	1680	−0.91
14JKC-3-12	145	0.053424	0.001729	0.282559	0.000011	0.282554	−7.5	−4.5	0.4	1000	1485	−0.95
Sample 14JKX-4: fine-grained granite												
14JKX-4-1	141	0.042258	0.001404	0.282548	0.000011	0.282544	−7.9	−5.0	0.4	1007	1509	−0.96
14JKX-4-2	141	0.097294	0.003013	0.282579	0.000009	0.282571	−6.8	−4.0	0.3	1006	1449	−0.91
14JKX-4-3	141	0.075267	0.002307	0.282525	0.000010	0.282519	−8.7	−5.9	0.3	1066	1567	−0.93
14JKX-4-4	141	0.060171	0.002024	0.282431	0.000013	0.282426	−12.1	−9.2	0.4	1193	1776	−0.94
14JKX-4-5	141	0.061236	0.001945	0.282490	0.000011	0.282485	−10.0	−7.1	0.4	1106	1644	−0.94
14JKX-4-6	141	0.062281	0.001928	0.282507	0.000010	0.282502	−9.4	−6.5	0.4	1080	1605	−0.94
14JKX-4-7	141	0.115385	0.003517	0.282492	0.000009	0.282483	−9.9	−7.1	0.3	1151	1647	−0.89
14JKX-4-8	141	0.118830	0.003653	0.282557	0.000012	0.282548	−7.6	−4.8	0.4	1057	1501	−0.89
14JKX-4-9	141	0.108175	0.003369	0.282575	0.000010	0.282566	−7.0	−4.2	0.4	1023	1461	−0.90
14JKX-4-10	141	0.069188	0.002070	0.282461	0.000010	0.282455	−11.0	−8.1	0.4	1151	1710	−0.94
14JKX-4-11	141	0.068753	0.002207	0.282554	0.000012	0.282548	−7.7	−4.8	0.4	1020	1501	−0.93
14JKX-4-12	141	0.113367	0.003506	0.282595	0.000010	0.282585	−6.3	−3.5	0.4	997	1417	−0.89
14JKX-4-13	141	0.091176	0.002802	0.282501	0.000011	0.282493	−9.6	−6.8	0.4	1116	1624	−0.92
14JKX-4-14	141	0.076863	0.002370	0.282521	0.000010	0.282514	−8.9	−6.0	0.3	1073	1577	−0.93
14JKX-4-15	141	0.058535	0.001875	0.282545	0.000009	0.282540	−8.0	−5.1	0.3	1024	1519	−0.94
14JKX-4-16	141	0.157286	0.004836	0.282492	0.000011	0.282479	−9.9	−7.3	0.4	1197	1655	−0.85
14JKX-4-17	141	0.046739	0.001513	0.282507	0.000009	0.282503	−9.4	−6.4	0.3	1067	1601	−0.95
14JKX-4-18	141	0.093533	0.002880	0.282554	0.000011	0.282546	−7.7	−4.9	0.4	1040	1505	−0.91
14JKX-4-19	141	0.054110	0.001750	0.282545	0.000010	0.282541	−8.0	−5.1	0.4	1020	1518	−0.95

$\varepsilon_{Hf}(t) = 10{,}000 \times (\{[(^{176}Hf/^{177}Hf)_S - (^{176}Lu/^{177}Hf)_S \times (e^{\lambda t} - 1)] / [(^{176}Hf/^{177}Hf)_{CHUR,0} - (^{176}Lu/^{177}Hf)_{CHUR} \times ((e^{\lambda t} - 1)] - 1\}$. $T_{DM1} = 1/\lambda \times \ln\{1 + [(^{176}Hf/^{177}Hf)_S - (^{176}Hf/^{177}Hf)_{DM}] / [(^{176}Hf/^{177}Hf)_S - (^{176}Hf/^{177}Hf)_{DM}]\}$. $T_{DM2} = T_{DM1} - (T_{DM1} - t) \times [(fcc - fs) / (fcc - f_{DM})]$. $f_{Lu/Hf} = (^{176}Lu/^{177}Hf)_S / (^{176}Lu/^{177}Hf)_{CHUR} - 1$, where, $\lambda = 1.867 \times 10^{-11}$/a (Söderlund et al., 2004); $(^{176}Lu/^{177}Hf)_S$ and $(^{176}Hf/^{177}Hf)_S$ are the measured values of the samples; $(^{176}Lu/^{177}Hf)_{CHUR} = 0.0332$ and $(^{176}Hf/^{177}Hf)_{CHUR,0} = 0.282772$ (Blichert-Toft and Albarede, 1997); $(^{176}Lu/^{177}Hf)_{DM} = 0.0384$ and $(^{176}Hf/^{177}Hf)_{DM} = 0.28325$ (Griffin et al., 2000); $(^{176}Lu/^{177}Hf)_{mean\ crust} = 0.015$; $fcc = [(^{176}Lu/^{177}Hf)_{mean\ crust} / (^{176}Lu/^{177}Hf)_{CHUR}] - 1$; $f_s = f_{Lu/Hf}$; $f_{DM} = [(^{176}Lu/^{177}Hf)DM / (^{176}Lu/^{177}Hf)_{CHUR}] - 1$; t = crystallization time of zircon.

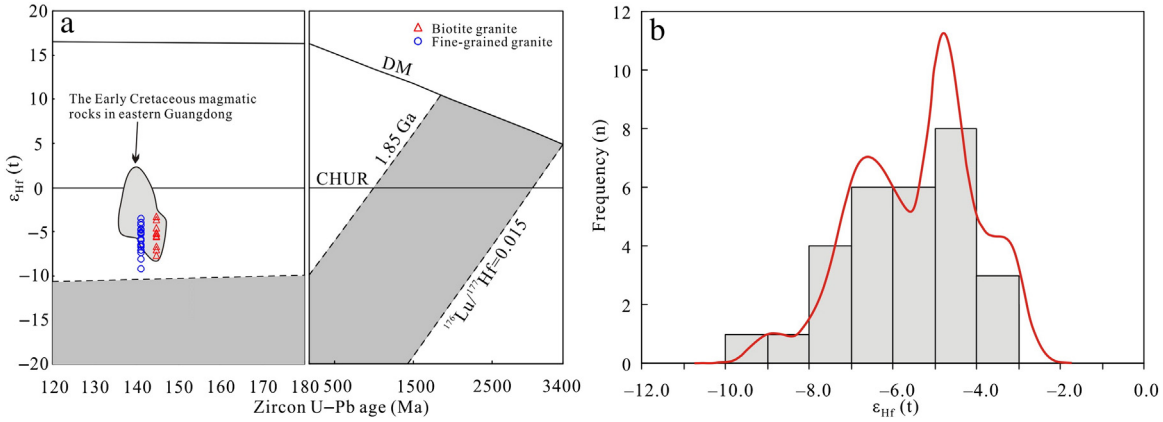

Fig. 13. (a) Diagram of $\varepsilon_{Hf}(t)$ vs. U–Pb ages for zircons from the Jinkeng granites with the shaded field indicating Hf isotope evolution for Cathaysia crustal basement (Xu et al., 2007; He and Xu, 2012). Background data for the Early Cretaceous intrusions and volcanics in eastern Guangdong are from Authors' unpublished data, Guo et al. (2012), Liu et al. (2015), Qiu et al. (2016a, b) and Zhou et al. (2016). (b) Histogram of $\varepsilon_{Hf}(t)$ for zircons from the Jinkeng granites.

Chondrite-normalized rare earth element (REE) concentrations of the Jinkeng granites are shown in Fig. 9a. They are characterized by relatively flat REE patterns ($(La/Yb)_N$ = 1.7–5.6, mean = 3.9), with low total REE contents of 60 to 183 ppm (mean = 144 ppm), and distinctly negative Eu anomalies (δEu = 0.05–0.19, mean = 0.11). In addition, primitive-mantle-normalized trace element data for the granites (Fig. 9b) show strong enrichments in Rb, Th, U, K, and Pb, and significant depletions in Ba, Sr, Ti, and P. The concentrations of high-field-strength elements (HFSE; e.g., Nb, Ta, and Zr) are low and K/Rb (128–179) values are low, whereas Rb/Sr (6–36) values are relatively high.

5.2. Biotite composition

Electron microprobe analyses and chemical formulae calculated for biotite from the granites are listed in Table 2. Chemical compositions of biotite from the porphyritic granodiorite are also listed for comparison. Biotites from the granites display high Fe/(Fe + Mg) values (0.95–0.99) and low MgO (0.15–0.97 wt.%), whereas biotites from the porphyritic granodiorite show relatively low Fe/(Fe + Mg) values (0.58–0.61), but high MgO (8.20–8.79 wt.%) contents. In the Mg–(Fe^{3+} + Al^{VI} + Ti)–(Fe^{2+} + Mn) diagram, biotites from the granites and the porphyritic granodiorite can be clarified as siderophyllite and ferri-biotite, respectively (Fig. 10a). In the Fe^{2+}–Fe^{3+}–Mg diagram, biotite data from the granites fall between QFM and NNO, whereas those of porphyritic granodiorite are above NNO (Fig. 10b).

5.3. Zircon U–Pb geochronology

Zircons from representative biotite granite (14JKC-3) and fine-grained granite (14JKX-4) samples are euhedral to subhedral, light yellow in color, transparent, and prismatic. Cathodoluminescence imaging (CL; Fig. 11) shows that the zircons are dark to slightly bright in appearance, and show concentric zoning. They are typically 80–200 μm in size, and have length:width ratios of 2:1–3:1. Thirty spots from biotite granite and 19 spots from fine-grained granite were analyzed (Table 3; Fig. 11), although some of these analyses were excluded because the data were highly discordant. The Th and U concentrations of zircons in the granite are variable, with Th = 221–4392 and U = 234–5668 ppm, and Th/U = 0.3–1.5 (mean = 0.8). These results, along with the zircon morphology, indicate that the zircons are of a magmatic origin (Hoskin and Schaltegger, 2003; Rubatto and Gebauer, 2000; Wu and Zheng, 2004). The concordant apparent $^{206}Pb/^{238}U$ ages of the biotite and fine-grained granites range from 141.2 ± 2.3 to 150.3 ± 2.7 Ma, and 135.2 ± 2.0 to 147.0 ± 1.8 Ma, with weighted mean $^{206}Pb/^{238}U$ ages of 144.7 ± 0.8 Ma (MSWD = 1.0, n = 26) and 141.1 ± 1.3 Ma (MSWD = 1.4, n = 19), respectively (Fig. 12). These weighted mean ages are identical within error, indicating that the biotite granite and fine-grained granite are coeval, as also suggested by their transitional relationship.

5.4. Zircon Hf isotopes

The spots used for U–Pb dating were also used for in situ zircon Hf isotope analysis (Table 4; Fig. 13). Ten analyses of biotite granite (sample 14JKC-3) yielded $^{176}Hf/^{177}Hf$ = 0.282475–0.282595, with $\varepsilon_{Hf}(t)$ values ranging from −7.6 to −3.3 and T_{DM2} = 1406–1680 Ma. Nineteen analyses of fine-grained granite (sample 14JKX-4) yielded variable $^{176}Hf/^{177}Hf$ values (0.282431–0.282595), with $\varepsilon_{Hf}(t)$ = −9.2 to −3.5 and T_{DM2} = 1417–1776 Ma.

5.5. Molybdenite Re–Os dating

The Re–Os data for eight molybdenite samples from the Jinkeng deposit are listed in Table 5. The data were plotted using ISOPLOT V.3.0

Table 5
Results of Re–Os dating of molybdenite from the Jinkeng deposit.

Sample no.	Weight (g)	Re (ppb)		^{187}Re (ppb)		Os^C (ppb)		$^{187}Os^T$ (ppb)		^{188}Os (ppb)		$^{187}Re/^{188}Os$		$^{187}Os/^{188}Os$	
		Measured	2σ	Measured	2σ	Measured	2σ	Measured	2σ	Measured	2σ	Measured	2σ	Measured	2σ
JKM-1	0.1215	1775.00	7.68	1115.66	4.83	0.281	0.040	2.640	0.025	0.037	0.005	30,371.15	4139.50	71.86	9.42
JKM-2	0.0742	3257.57	9.66	2047.51	6.07	0.366	0.005	4.851	0.017	0.048	0.001	42,809.11	445.48	101.42	0.99
JKM-3	0.1237	238.26	0.78	149.75	0.49	0.131	0.001	0.382	0.003	0.017	0.000	8744.49	26.85	22.29	0.04
JKM-4	0.1207	702.99	2.91	441.85	1.83	0.124	0.020	1.075	0.004	0.016	0.003	27,185.75	4323.95	66.11	10.52
JKM-5	0.121	232.93	1.12	146.40	0.70	0.120	0.021	0.377	0.001	0.016	0.003	9353.80	1571.29	24.05	4.07
JKM-6	0.1207	231.89	0.76	145.75	0.48	0.112	0.020	0.373	0.003	0.015	0.003	9977.25	1759.60	25.51	4.40
JKM-7	0.1219	242.41	1.16	152.36	0.73	0.091	0.018	0.382	0.001	0.012	0.002	12,758.23	2447.34	31.97	6.21
JKM-8	0.1654	109.28	0.55	68.69	0.35	0.088	0.011	0.188	0.001	0.012	0.002	6006.56	757.14	16.45	2.05

Note: Os^C represents common Os; $^{187}Os^T$ represents total ^{187}Os.

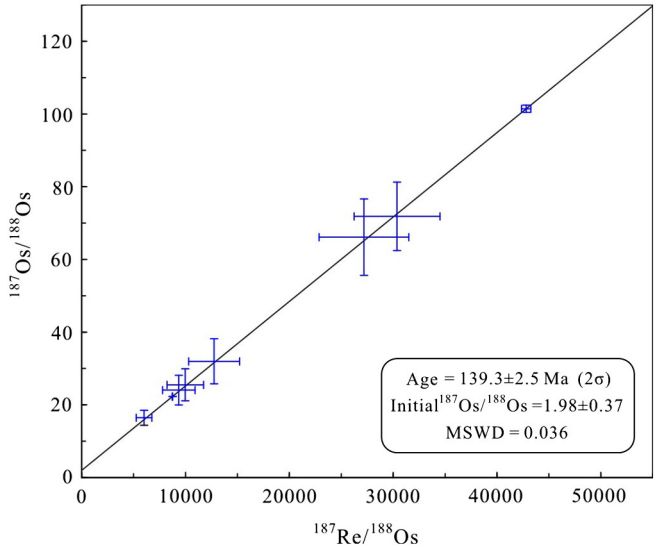

Fig. 14. Molybdenite Re–Os isochron age for cassiterite–bearing veins within the Jinkeng deposit.

(Ludwig, 2003) and show a linear correlation (Fig. 14), yielding an isochron age of 139.3 ± 2.5 Ma with an initial $^{187}Os/^{188}Os$ value of 1.98 ± 0.37 (2σ, MSWD = 0.036). This age is considered to be representative of the mineralization age in the deposit.

6. Discussion

6.1. Timing of magmatism and mineralization

The zircon U–Pb ages of the biotite (144.7 ± 0.8 Ma) and fine-grained (141.1 ± 1.3 Ma) granites associated with the Jinkeng deposit indicate that the granite pluton was emplaced during the Early Cretaceous. The similarity of these ages with the Re–Os isochron age of 139.3 ± 2.5 Ma for molybdenite samples from the cassiterite–arsenopyrite–molybdenite veins suggests that polymetallic mineralization at Jinkeng is genetically related to the emplacement of the biotite granite and fine-grained granite pluton.

Magmatism in eastern Guangdong occurred during the Middle Jurassic to Early Cretaceous, with major episodes occurring at 170–150 Ma and 145–135 Ma (Fig. 15; Table 6). Mineralization in the area has been dated at 145–135 Ma (Early Cretaceous), with a less significant episode occurring from 160 to 150 Ma (Late Jurassic; Fig. 15; Table 6).

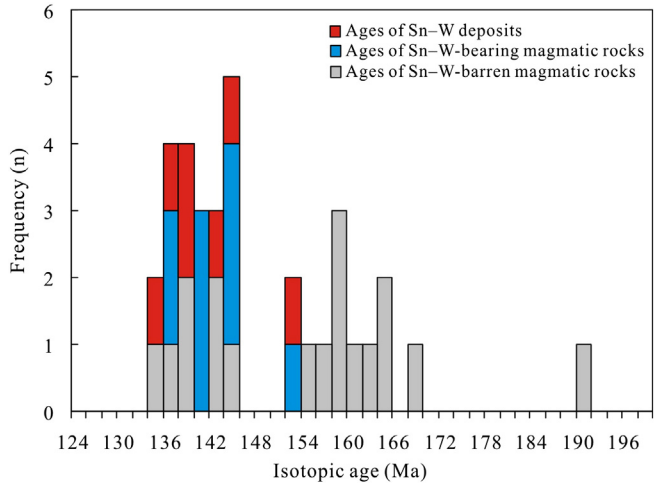

Fig. 15. Histogram of the isotopic ages of Sn (W) deposits, Sn (W)-bearing magmatic rocks, and Sn (W)-barren magmatic rocks within eastern Guangdong Province. The Jinkeng data are from this study, unpublished data of the authors are used for the Taoxihu, Tashan and Dadaoshan deposits, and the remaining data are from Guo et al. (2012), Li et al. (2016), Liu et al. (2015), Ni et al. (1983), Qiu et al., (in press, 2016), Xu and Yue (1999a), Zhang et al. (2015), Zhao et al. (2012) and Zhou et al., 2016 (Table 6).

The Sn–W mineralization in Nanling and surrounds is associated with distinct episodes in the Late Triassic (230–210 Ma), Late Jurassic (160–150 Ma), and Cretaceous (134–80 Ma; Chen et al., 2008; Hu and Zhou, 2012; Hua et al., 2010; Mao et al., 2008, 2013a). However, several Sn–W deposits in the region have been dated at 145–135 Ma, including the Jubankeng W–Sn deposit in northern Guangdong (139.2 ± 1.5 Ma; Fu et al., 2009), Bailashui Sn deposit in southern Hunan (137 ± 5 Ma; Li et al., 2006), Dajishan W deposit in southern Jiangxi (144.0 ± 0.7 Ma; Zhang et al., 2006), and Dahutang W deposit in northern Jiangxi (139.2 ± 1.0 Ma; Mao et al., 2013b). This, together with the abundance of Sn–W deposits in eastern Guangdong with ages of 145–135 Ma, suggest that a significant Sn–W mineralization event occurred between 145 and 135 Ma in southern China.

6.2. Petrogenesis of the Jinkeng granites and implications for Sn mineralization

6.2.1. Classification of the Jinkeng granites

The Jinkeng granites contain high concentrations of SiO_2 and total alkalis, and low concentrations of Fe, Mg, Ca, and P. Compared with primitive mantle, and relatively unfractionated porphyritic granodiorites in the area, they are enriched in Rb, Th, U, and Pb, depleted in Ba, Sr, and Ti, have well-developed negative Eu anomalies, high Rb/Sr, and low K/Rb. These characteristics are indicative of formation from a highly fractionated granitic magma (Fig. 16a), and fractional crystallization may have resulted in the precipitation of biotite, apatite, Fe–Ti oxides (e.g., ilmenite and titanite), and plagioclase (Clemens, 2003; Foley et al., 2000; Sylvester, 1998; Xiong et al., 2005). The relatively low concentrations of Ba, Zr, Y, Nb, La, Ce (Zr + Nb + Ce + Y < 284 ppm), and the other REE, and low zircon saturation temperatures (Watson and Harrison, 1983; 749–787 °C; Table 1) of the Jinkeng granites are distinct from A-type granites (Bonin, 2007; Dall'Agnol and Oliveira, 2007; Whalen et al., 1987). Furthermore, the granites are weakly peraluminous with A/CNK < 1.1, thus differing from S-type granites, which are typically strongly peraluminous with A/CNK values >1.1 (Chappell and White, 1974; Clemens, 2003; Wu et al., 2007). The very low concentrations of P_2O_5 (≤0.10 wt.%) in the Jinkeng granites correlate negatively with SiO_2 (Fig. 16b), and Th and Y correlate positively with Rb, which are features consistent with the fractionation trends of I-type magmas (Fig. 16c, d; Chappell, 1999; Li et al., 2007a, 2007b; Wu et al., 2003a, 2003b). Thus, we conclude that the Jinkeng granites are highly fractionated I-type granites, similar to other Late Jurassic to Early Cretaceous highly fractionated I-type granites in southern China (e.g., Fogang, Baishigang, Longyuanba, Pengshan, Taoxihu, and Mantoushan plutons; Li et al., 2007a; Qiu et al., 2005, 2016a; Tao et al., 2013; Xu et al., 2016; Zhang et al., 2015).

6.2.2. Petrogenesis of the Jinkeng granites

Parental magmas of highly fractionated I-type granites may be produced by (1) fractional crystallization from mafic melts (Chappell, 1999; Wyborn et al., 2001), or (2) partial melting of crustal material (Chappell, 1999; Chappell et al., 2012). The Jinkeng granites have a relatively narrow range of compositions and, although granitoids are widespread throughout eastern Guangdong, the occurrence mafic rocks in the area is minor, thus it is unlikely that these granites represent the products of fractional crystallization (Chappell, 1999). They have relatively low Nb/Ta (9–13, mean = 11), Zr/Hf (22–27, mean = 24), and Th/U values (2–6, mean = 4; Table 1) that are close to average crustal compositions (Nb/Ta = 11, Zr/Hf = 33, and Th/U = 4; Taylor and Mclennan, 1985), suggesting a crustal source for the magma. The zircons in the biotite and fine-grained granites have negative $\varepsilon_{Hf}(t)$ values ranging from −7.6 to −3.3 and −9.2 to −3.5, respectively, and yield two-stage Hf model ages (T_{DM2}) of 1406–1680 and 1417–

Table 6
Ages of igneous rocks and W–Sn polymetallic mineralization, and Hf isotopic compositions of magmatic rocks in eastern Guangdong.

Deposit/pluton	Lithology	Measured objects	Method	Age (Ma)	$\varepsilon_{Hf}(t)$	T_{DM2} (Ma)	Reference
Jinkeng Sn polymetallic deposit	Biotite granite	Zircon	LA–ICPMS U–Pb	144.7 ± 0.8	−7.6 to −3.3	1406–1680	This study
	Fine-grained granite	Zircon	LA–ICPMS U–Pb	141.1 ± 1.3	−9.2 to −3.5	1417–1776	
		Molybdenite	Re–Os isochron	139.3 ± 2.5			
Taoxihu Sn polymetallic deposit	Granite porphyry	Zircon	LA–ICPMS U–Pb	141.8 ± 1.0	−10.5 to −5.9	1566–1863	Qiu et al. (2016a)
		Molybdenite	Re–Os isochron	139.0 ± 0.8			Authors' unpublished data
Tashan Sn polymetallic deposit	Granite porphyry	Zircon	LA–ICPMS U–Pb	136.8 ± 1.1	−4.9 to −2.1	1322–1507	Authors' unpublished data
		Cassiterite	LA–ICPMS U–Pb	136.5 ± 8.1			
Changpu Sn polymetallic deposit	Quartz porphyry	Zircon	LA–ICPMS U–Pb	145.0 ± 0.9	−8.0 to −2.7	1371–1704	Qiu et al. (2016b)
Tiandong W–Sn deposit	Medium-grained granite	Zircon	LA–ICPMS U–Pb	191.5 ± 0.9	+4.0 to +9.8	611–975	Liu et al. (2015)
	Coarse-grained granite	Zircon	LA–ICPMS U–Pb	158.0 ± 1.3	−3.6 to −0.1	1217–1439	
	Fine-grained biotite granite	Zircon	LA–ICPMS U–Pb	140.5 ± 0.8	−5.4 to −1.6	1330–1423	
		Molybdenite	Re–Os isochron	142.6 ± 6.3			Li et al. (2016)
Hopoao Sn polymetallic deposit	Monzogranite	Whole rock	Rb–Sr ischron	144.9 ± 9.4			Xu and Yue (1999a)
		Sericite	Ar–Ar isochron	145.4 ± 1.9			
Lianhuashan W deposit	Biotite granite	Whole rock	Rb–Sr ischron	137.2 ± 2.5			Ni et al. (1983)
		Muscovite	Rb–Sr isochron	135			
Dadaoshan Sn deposit	Porphyritic granite	Zircon	LA–ICPMS U–Pb	153.2 ± 1.2			Authors' unpublished data
		Molybdenite	Re–Os isochron	152.8 ± 7.8			
Mantoushan	Syeno-monzogranites and alkali feldspar granites	Zircon	LA–ICPMS U–Pb	166–161	−7.4 to −3.2	1260–1480	Zhou et al. (2016)
Hulutian	Alkali feldspar granites	Zircon	LA–ICPMS U–Pb	139 ± 2	−0.7 to +1.8	960–1100	
Longwo	Granodiorite	Zircon	LA–ICPMS U–Pb	165.2 ± 1.9	−4.6 to −0.9	1272–2166	Zhang et al. (2015)
Lianhuashan	Granodiorite	Zircon	SIMS U–Pb	154.3 ± 1.4	−6.5 to −3.6	1432–1614	
Wushikeng	Biotite granite	Zircon	LA–ICPMS U–Pb	159.7 ± 1.7	−4.0 to +3.9	962–1466	
Shigushan	Biotite granite	Zircon	SIMS U–Pb	158.5 ± 1.3	−5.1 to −2.5	1366–1538	
Chiliao	Biotite granite	Zircon	LA–ICPMS U–Pb	157.2 ± 1.8	−5.6 to −3.2	1408–1565	
Fenghuang	Biotite granite	Zircon	LA–ICPMS U–Pb	161.3 ± 1.2	−3.9 to −0.3	1228–1457	
Dabu	Biotite granite	Zircon	LA–ICPMS U–Pb	136.3 ± 0.6			Zhao et al. (2012)
Jiexi	Biotite-K-spar granite	Zircon	LA–ICPMS U–Pb	134.9 ± 0.4			
Douling Formation in Fengshun basin	Dacite	Zircon	LA–ICPMS U–Pb	168.2 ± 2.0	−7.8 to −3.8	1463–1714	Guo et al. (2012)
	Rhyolite	Zircon	LA–ICPMS U–Pb	142.7 ± 1.0	−6.5 to +0.3	1243–1621	
	Dacite	Zircon	LA–ICPMS U–Pb	165.0 ± 1.0	−3.9 to +1.5	1219–1475	
	Rhyolite	Zircon	LA–ICPMS U–Pb	145.8 ± 2.0			
	Dacite	Zircon	LA–ICPMS U–Pb	143.3 ± 0.5			
	Dacite	Zircon	SIMS U–Pb	139.0 ± 1.0	−2.8 to +2.3	1230–1372	

1776 Ma, respectively. These Hf isotopic characteristics are similar to those of Early Cretaceous (145–135 Ma) granitoids and volcanic rocks in eastern Guangdong (Fig. 13; Author's unpublished data; Guo et al., 2012; Liu et al., 2015; Qiu et al., 2016a, b; Zhou et al., 2016). Furthermore, the Hf isotopic data fall beneath or slightly above the chondrite line, and above the domain of Cathaysia crustal basement rocks (Fig. 13a), suggesting that the magma was derived from a crustal source, and contained variable amounts of mantle-derived material. Although ancient basement rocks have not been identified in eastern Guangdong, previously published whole-rock and Sr–Nd–Pb–Hf isotopic data of magmatic rocks in the area have indicated that the basement is composed of meta-igneous and metasedimentary rocks (Guo et al., 2012; Lei and Yue, 1993; Xu and Yue, 1999b). Therefore, since the Jinkeng granites are overall slightly peraluminous (Fig. 8b), it is likely that the magma source contained meta-igneous rocks, and some proportion of metasedimentary material. Thus, we conclude that the Jinkeng granites were derived from the partial melting of a Mesoproterozoic crustal source, with minor input of mantle-derived melts.

6.2.3. Implications for Sn mineralization in the Jinkeng deposit

Field observations and the ages of the Jinkeng granites and Sn mineralization indicate a spatial and temporal association between the two. In addition, these F-specialized granites (F: 330–2520 ppm, averaging, 1328 ppm, Table 1) belong to typical Sn-bearing granites due to relatively high Sn contents varying from 8 to 30 ppm (averaging, 12 ppm) (Table 1), which are higher than average upper crustal and lower crustal values (5.5 ppm and 1.5 ppm, respectively) (Taylor and Mclennan, 1985).

Studies suggest that fractional crystallization is a very important process in the formation of Sn-bearing granites, since it causes the enrichment of incompatible elements, such as Sn (Blevin and Chappell, 1995; Breiter, 2012; Fogliata et al., 2012; Gomes and Neiva, 2002; Lehmann and Harmanto, 1990; Teixeira et al., 2012; Xu et al., 2016). For example, the mineralized Sn granites of the Pengshan deposit (Xu et al., 2016), Dulong polymetallic deposit (Xu et al., 2015) in southern China, granites associated with Sn–W mineralization in the Krušné hory/Erzgebirge Mountains in central Europe (Breiter, 2012), and Sierras Pampeanas Orogen of NW Argentina (Fogliata et al., 2012) are all highly differentiated. Therefore, extensive fractional crystallization in the Jinkeng granites may have played a key role in the formation of the deposit. Oxygen fugacity of a magma also controls the enrichment of Sn. Typically, Sn concentrates in the residual melt as Sn^{2+} under reduced conditions, whereas it is removed as Sn^{4+} in early crystallizing phases (magnetite and titanite) under oxidized conditions (Cobbing et al., 1986; Linnen et al., 1996). The composition of biotite in the Jinkeng granites falls below the NNO buffer (Fig. 10b), suggesting they crystallized under relatively reduced conditions, which would have facilitated the enrichment of Sn in a late hydrothermal fluid.

In contrast to the biotite and fine-grained granites, the porphyritic granodiorite at Jinkeng is relatively unfractionated (SiO_2 < 66 wt.%, Rb/Sr < 1; Fig. 9; Author's unpublished data). The biotites in the porphyritic granodiorite show extreme depletions in F (≤0.04 wt.%; Table 2) and a relatively high oxygen fugacity (above the NNO buffer; Fig. 10b). Therefore, the porphyritic granodiorite is distinct from typical Sn-bearing granites. In addition, some of the Sn-rich orebodies are located along NW-trending faults that crosscut the granodiorite. Furthermore, the Jinkeng Sn-bearing granites have intruded into the porphyritic granodiorite, and geochronological data indicate that the granodiorite predates the granites and Sn mineralization. Therefore, we conclude that the porphyritic granodiorite hosts orebodies, but is not itself enriched in Sn.

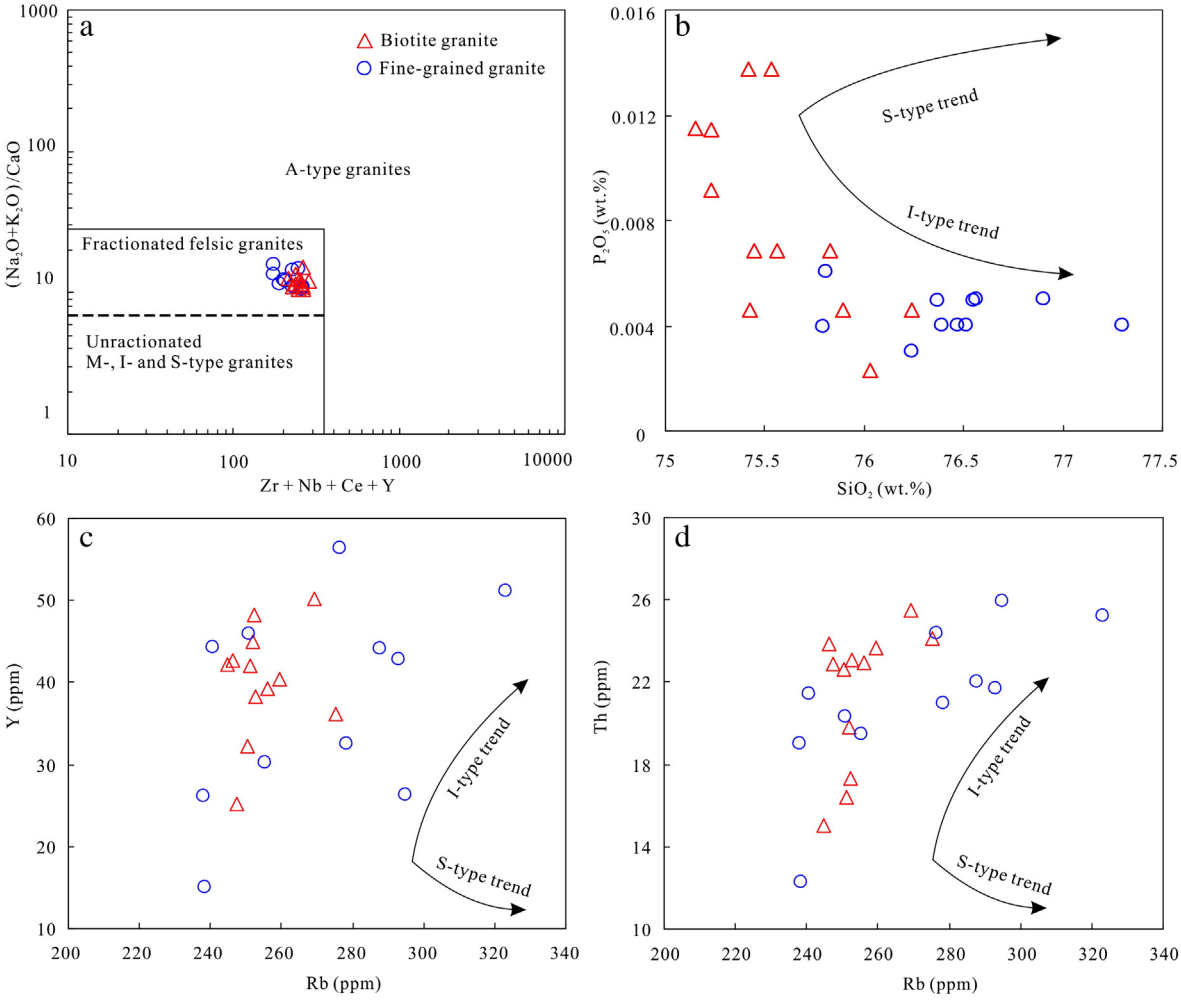

Fig. 16. (a) ($K_2O + Na_2O$)/CaO vs. Zr + Nb + Ce + Y (Whalen et al., 1987), (b) P_2O_5 vs. SiO_2, (c) Y vs. Rb and (d) Th vs. Rb diagrams for samples of Jinkeng granites. I- and S-type granite compositional trends are from Li et al. (2007a) and Wu et al. (2003a).

6.2.4. Comparison with other Mesozoic Sn-bearing granites in southern China

The Mesozoic Sn mineralization in southern China is associated with different types of granitoids (S-type, A-type, and highly fractionated I-type granites), which are different from each other in terms of their mineral composition, geochemistry, and ore productivity (Table 7; Fig. 9). The highly fractionated I-type Jinkeng Sn-bearing granites are characterized by low oxygen fugacity, and are weakly peraluminous (A/CNK = 1.0–1.1) high-K calc-alkaline, with high SiO_2 (74.6–76.7 wt.%), Rb/Sr (6–36), and relatively low ΣREE (60–183 ppm), LREE/HREE (2.4–5.5), Ti (373–566 ppm), P (10–60 ppm), and well-developed negative Eu anomalies (δEu = 0.05–0.19). These features are similar to those of the Early Cretaceous highly fractionated I-type Pengshan Sn-bearing granites, which, in addition to their low oxygen fugacity, and weakly peraluminous (A/CNK = 1.0–1.1), high-K calc-alkaline characteristics, have high SiO_2 (75.4–76.5 wt.%), Rb/Sr (8–50), and low ΣREE (41–85 ppm), LREE/HREE (2.4–3.3), Ti (599–839 ppm), and P (262–349 ppm), with distinct negative Eu anomalies (δEu = 0.04–0.12; Xu et al., 2016). They do, however, differ from the Late Cretaceous Laojunshan S-type Sn-bearing granites (Feng et al., 2012; Xu et al., 2015), and the Late Jurassic Huashan–Guposhan–Qitianling A-type Sn-bearing granites (Jiang et al., 2008; Shu et al., 2011; Wang et al., 2013; Zhu et al., 2006). The Laojunshan granites are characterized by low oxygen fugacity, and are strongly peraluminous (A/CNK = 1.1–1.4), high-K calc-alkaline rocks, with high SiO_2 (71.9–74.2 wt.%), Rb/Sr (6–10), Ti (659–1079 ppm), P (830–1223 ppm), LREE/HREE (8.5–10.9), and low ΣREE (81–125 ppm), and small negative Eu anomalies (δEu = 0.20–0.32; Feng et al., 2012; Xu et al., 2015). In comparison, the Huashan–Guposhan–Qitianling granites have relatively high oxygen fugacity, are metaluminous to weakly peraluminous (A/CNK = 0.9–1.1), showing a shoshonitic affinity, with a wide range of SiO_2 (66.7–76.9 wt.%) values, high ΣREE (96–626 ppm), LREE/HREE (2.3–16.4), Ti (599–5336 ppm), and P (87–1223 ppm), relatively lower Rb/Sr (1 − 12), and negative Eu anomalies (δEu = 0.11–0.45; Jiang et al., 2008; Shu et al., 2011; Wang et al., 2013; Zhu et al., 2006).

6.3. Geodynamic setting

Mesozoic tectono-magmatic and associated metallogenesis in southern China were associated with regional extension triggered by the subduction of the paleo-Pacific Plate beneath the South China Block, beginning in the Early or Middle Jurassic (e.g., Charvet et al., 1994; Hua et al., 2005; Jiang et al., 2015; Lapierre et al., 1997; Li and Li, 2007; Li et al., 2007a; Mao et al., 2013a; Wong et al., 2009; Zhou and Li, 2000; Zhou et al., 2006). Abundant A-type granitic and within-plate basaltic magmatism occurred during the Early Cretaceous (139–122 Ma), indicating that extension, likely induced by the rollback of the subducted paleo-Pacific Plate, was occurring at this time (Jiang et

Table 7
Comparison between Jinkeng Sn-bearing granites and other S-type, A-type and highly fractionated I-type Sn-bearing granites in South China.

Location	Pluton	Petrography	Genetic type	Age (Ma)	Geochemical features	Isotope	Model age	Ore productivity	References
Eastern Guangdong	Jinkeng granites	Biotite granite	Highly fractionated I-type granites	141–144	Low oxygen fugacity, weakly peraluminous (A/CNK = 1.0–1.1) and high-K calc-alkine series, with high SiO_2 (74.6–76.7 wt.%), Rb/Sr (6–36), and relatively low ΣREE (60–183 ppm), LREE/HREE (2.4–5.5), Ti (373–566 ppm), P (10–60 ppm), and significant negative Eu anomalies (δEu = 0.05–0.19).	ε_{Hf} (t) = −9.2 to −3.3	T_{DM2} = 1.41–1.78 Ga	Cassiterite-sulfide-type Sn, Cu, Pb, Zn mineralzaition	This study
Northern Jiangxi	Pengshan granites	Fine-grained biotite monzogranite	Highly fractionated I-type granites	128–129	Low oxygen fugacity, weakly peraluminous (A/CNK = 1.0–1.1) and high-K calc-alkine series, with high SiO_2 (75.4–76.5 wt.%), Rb/Sr (8–50), and low ΣREE (41–85 ppm), LREE/HREE (2.4–3.3), Ti (599–839 ppm), P (262–349 ppm) and sharply negative Eu anomalies (δEu = 0.04–0.12).	ε_{Hf} (t) = −4.5 to +0.5	T_{DM2} = 1.15–1.47 Ga	Skarn-type Sn, Pb, Zn mineralization	Xu et al. (2016)
Southeastern Yunnan	Laojunshan granites	Two mica monzogranite and porphyritic granite	S-type granites	86–90	Low oxygen fugacity, strongly peraluminous (A/CNK = 1.1–1.4) and high-K calc-alkine series, with high SiO_2 (71.9–74.2 wt.%), Rb/Sr (6–10), Ti (659–1079 ppm), P (830–1223 ppm), LREE/HREE (8.5–10.9), and low ΣREE (81–125 ppm), and relatively negative Eu anomalies (δEu = 0.20–0.32).	ε_{Hf} (t) = −15.5 to −2.5	T_{DM2} = 1.31–2.12 Ga	Greisen-, skarn-, manto-type Sn, W, Cu, Pb, Zn mineralization	Feng et al. (2012), Xu et al. (2015)
Southern Hunan and northern Guangxi	Huashan-Guposhan-Qitianling granites	Amphibole-biotite granite and biotite granite	A-type granites	151–163	Relatively high oxygen fugacity, metaluminous to weakly peraluminous (A/CNK = 0.9–1.1) and mostly shoshonite, with a wide range of SiO_2 (66.7–76.9 wt.%), high ΣREE (96–626 ppm), LREE/HREE (2.3–16.4), Ti (599–5336 ppm), P (87–1223 ppm), and relatively lower Rb/Sr (1–12), and negative Eu anomalies (δEu = 0.11–0.45).	ε_{Hf} (t) = −9.8 to +2.3	T_{DM2} = 1.03–1.82 Ga	Greisen-, quartz vein-, skarn-, cassiterite-sulfide- type Sn, W, Mo, Bi, Nb, Ta, Pb, Zn mineralzaition	Jiang et al. (2008), Shu et al. (2011), Wang et al. (2013), Zhu et al. (2006)

al., 2011, 2015; Li et al., 2015; Sun et al., 2015; Yan et al., 2015; Yang et al., 2011, 2012). The 140–125 Ma interval is also considered to be one of the significant extension-related mineralization episodes in southern China (Mao et al., 2004). More recently, Liu et al. (2016) proposed an asynchronous paleo-Pacific slab rollback model, occurring from 145 to 118 Ma, to account for the episodic magmatism and crustal extension in southeasten China. Thus, we conclude that lithospheric extension in the Early Cretaceous, which was caused by slab rollback, initiated at ~140 Ma.

High-K calc-alkaline I-type granites can be generated in continental arc or post-collision extensional settings (e.g., Altherr et al., 2000; Karsli et al., 2010; Pitcher, 1987; Roberts and Clemens, 1993; Topuz et al., 2010). Guo et al. (2012) proposed that the Late Jurassic–Early Cretaceous high-K calk-alkaline silicic lavas coeval with granitoids in eastern Guangdong formed in an extensional environment rather than an arc setting. Later, Zhou et al. (2016) suggested that the highly fractionated Early Cretaceous I-type granites (~140 Ma) in eastern Guangdong were formed in a back-arc extensional tectonic setting that was triggered by slab rollback. More recently, some Early Cretaceous mafic rocks and A-type granites in eastern Guangdong, considered to be associated with regional extension, have also been recognized (Authors' unpublished data). Furthermore, the Jinkeng Sn-bearing granites are geochemically dissimilar to typical arc magmas, showing no apparent negative Nb and Ta anomalies (e.g., De Astis et al., 2000). They are post-collisional granites (Fig. 17), indicating that the Sn-bearing granites also formed in an extensional environment. Therefore, we propose that the Jinkeng Sn-bearing granites and associated polymetallic mineralization were produced in an extensional tectonic setting, which likely developed from the rollback of the paleo-Pacific Plate at ~140 Ma. Such an extensional tectonic setting might also be responsible for the Early Cretaceous (145–135 Ma) Sn–W mineralization event in eastern Guangdong.

7. Conclusions

Based on new geochemical and age data for the Jinkeng Sn polymetallic deposit, we conclude that:

(1) Hydrothermal vein-type Sn polymetallic mineralization in the deposit is associated with granites that were emplaced during the Early Cretaceous (~140 Ma).
(2) Geochemical and Hf isotope data indicate that the Jinkeng granites are highly fractionated I-type granites that were derived from the partial melting of a Proterozoic crustal source, with minor input from the mantle.
(3) Both the highly fractionated I-type granites and the associated mineralization in the Jinkeng deposit formed in an extensional environment, which was likely caused by the rollback of the paleo-Pacific Plate at ~140 Ma.

Acknowledgments

This research was financially supported by China Geological Survey Package Exploration Key Basic Geology Research Project (Grant No. 12120114015901). We express our gratitude to Prof. Franco Pirajno, Prof. Guoxiang Chi and anonymous reviewers for their critical reviews and excellent suggestions. We also thank Prof. Hecai Niu for his constructive suggestions. We thank the staff of Geology Bureau for Nonferrous Metals of Guangdong Province. State Key Laboratory of Isotope Geochemistry, Guangzhou Institute of Geochemistry, Chinese Academy of Sciences (GIG-CAS), and CAS Key Laboratory of Mineralogy and Metallogeny, GIG-CAS are thanked for LA–ICPMS zircon U–Pb dating, Hf isotope analyses, major and trace element analyses, mineral chemistry analyses, and Re–Os dating.

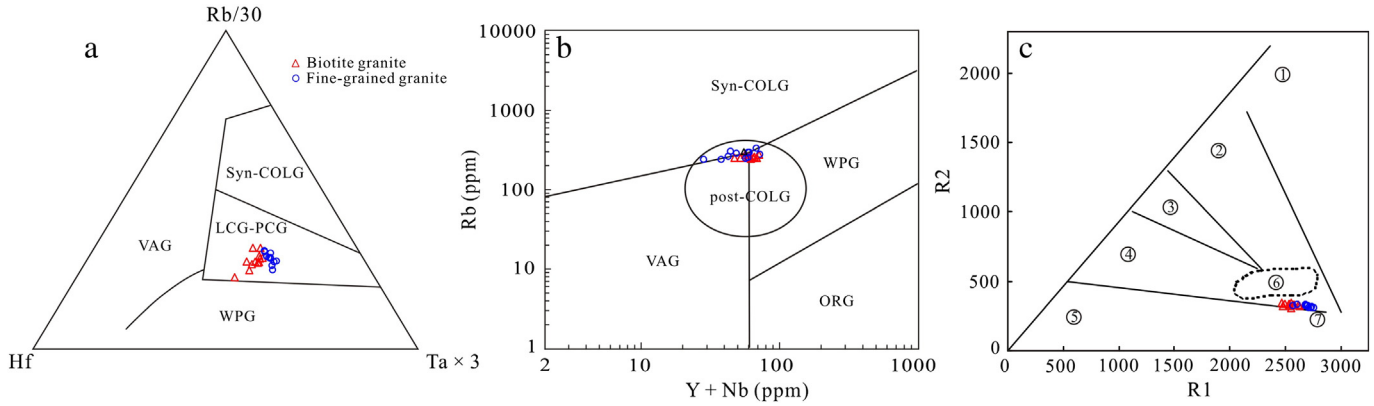

Fig. 17. (a) (Rb/30)–Hf–Ta × 3 (Harris et al., 1986), (b) Rb–(Y + Nb) (Pearce, 1996) and (c) R1–R2 (Batchelor and Bowden, 1985) diagrams for samples from the Jinkeng granites. Syn-COLG = syn-collision granite, VAG = volcanic-arc granite, WPG = within-plate granite, ORG = ocean-ridge granite, LCG = late-collision granite, PCG/post-COLG = post-collision granite, (1) = mantle-derived granite, (2) pre-plate-collision granite, (3) post-collisional-uplift granite, (4) late-orogenic granite, (5) anorogenic granite, (6) syn-collisional granite, (7) post-orogenic granite.

References

Altherr, R., Holl, A., Hegner, E., Langer, C., Kreuzer, H., 2000. High-potassium, calcalkaline I-type plutonism in the European Variscides: northern Vosges (France) and northern Schwarzwald (Germany). Lithos 50, 51–73.

Andersen, T., 2002. Correction of common lead in U–Pb analyses that do not report ^{204}Pb. Chem. Geol. 192, 59–79.

Batchelor, R.A., Bowden, P., 1985. Petrogenetic interpretation of granitoid rock series using multicationic parameters. Chem. Geol. 48, 43–55.

Black, L.P., Kamo, S.L., Allen, C.M., Aleinikoff, J.N., Davis, D.W., Korsch, R.J., Foudoulis, C., 2003. TEMORA 1: a new zircon standard for Phanerozoic U–Pb geochronology. Chem. Geol. 200, 155–170.

Blevin, P.L., Chappell, B.W., 1995. Chemistry, origin, and evolution of mineralized granites in the Lachlan fold belt, Australia; the metallogeny of I-and S-type granites. Econ. Geol. 90, 1604–1619.

Blichert-Toft, J., Albarede, F., 1997. The Lu–Hf isotope geochemistry of chondrites and the evolution of the mantle-crust system. Earth Planet. Sci. Lett. 148, 243–258.

Bonin, B., 2007. A-type granites and related rocks: evolution of a concept, problems and prospects. Lithos 97, 1–29.

Breiter, K., 2012. Nearly contemporaneous evolution of the A- and S-type fractionated granites in the Krušné hory/Erzgebirge Mts., Central Europe. Lithos 151, 105–121.

Chappell, B.W., 1999. Aluminium saturation in I- and S-type granites and the characterization of fractionated haplogranites. Lithos 46, 535–551.

Chappell, B.W., White, A.J.R., 1974. Two contrasting granite types. Pac. Geol. 8, 173–174.

Chappell, B.W., Bryant, C.J., Wyborn, D., 2012. Peraluminous I-type granites. Lithos 153, 142–153.

Charvet, J., Lapierre, H., Yu, Y., 1994. Geodynamic significance of the Mesozoic volcanism of southeastern China. J. SE Asian Earth Sci. 9, 387–396.

Chen, J., Lu, J.J., Chen, W.F., Wang, R.C., Ma, D.S., Zhu, J.C., Zhang, W.L., Ji, J.F., 2008. W–Sn–Nb–Ta-bearing granites in the Nanling Range and their relationship to metallogenesis. Geol. J. China Univ. 14, 459–473 (in Chinese with English abstract).

Clemens, J.D., 2003. S-type granitic magmas—petrogenetic issues, models and evidence. Earth Sci. Rev. 61, 1–18.

Cobbing, E.J., Mallick, D., Pitfield, P., Teoh, L.H., 1986. The granites of the southeast Asian tin belt. J. Geol. Soc. 143, 537–550.

Dall'Agnol, R., Oliveira, D.C., 2007. Oxidized, magnetite-series, rapakivi-type granites of Carajás, Brazil: implications for classification and petrogenesis of A-type granites. Lithos 93, 215–233.

De Astis, G., Peccerillo, A., Kempton, P.D., La Volpe, L., Wu, T.W., 2000. Transition from calc-alkaline to potassium-rich magmatism in subduction environments: geochemical and Sr, Nd, Pb isotopic constraints from the island of Vulcano (Aeolian arc). Contrib. Mineral. Petrol. 139, 684–703.

Feng, J.R., Mao, J.W., Pei, R.F., 2012. Ages and geochemistry of Laojunshan granites in sourtheastern Yunnan, China: implication for W–Sn–Pb–Zn polymetallic ore deposits. Mineral. Petrol. 107, 1–17.

Fogliata, A.S., Báez, M.A., Hagemann, S.G., Santos, J.O., Sardi, F., 2012. Post-orogenic, carboniferous granite-hosted Sn–W mineralization in the Sierras Pampeanas Orogen, northwestern Argentina. Ore Geol. Rev. 45, 16–32.

Foley, S.F., Barth, M.G., Jenner, G.A., 2000. Rutile/melt partition coefficients for trace elements and an assessment of the influence of rutile on the trace element characteristics of subduction zone magmas. Geochim. Cosmochim. Acta 64, 933–938.

Foster, M.D., 1960. Interpretation of the composition of trioctahedral mica. U.S. Geol. Surv. Prof. Pap. 354-B, 11–48.

Fu, J.M., Li, X.N., Cheng, S.B., Xu, D.M., Ma, L.Y., Chen, X.Q., 2009. Metallogenic ages of tungsten-tin polymetallic deposits in Lianping area, northern Guangdong Province. Geol. China 36, 1331–1339 (in Chinese with English abstract).

Gomes, M., Neiva, A., 2002. Petrogenesis of tin-bearing granites from Ervedosa, northern Portugal: the importance of magmatic processes. Chem. Erde-Geochem. 62, 47–72.

Griffin, W.L., Pearson, N., Belousova, E., Jackson, S., Van Achterbergh, E., O'Reilly, S.Y., Shee, S., 2000. The Hf isotope composition of cratonic mantle: LA-MC-ICP-MS analysis of zircon megacrysts in kimberlites. Geochim. Cosmochim. Acta 64, 133–147.

Griffin, W.L., Wang, X., Jackson, S.E., Pearson, N.J., O'Reilly, S.Y., 2002. Zircon geochemistry and magma mixing, SE China: in-situ analysis of Hf isotopes, Tonglu and Pingtan igneous complexes. Lithos 61, 237–269.

Guangdong Nonferrous Metals Geological Bureau 931 Team (GNMGB), 2015M. Reconnaissance Report of the Jinkeng Sn Polymetallic Deposit in Jiexi County, Guangdong Province. Unpublished Report. pp. 1–108 (in Chinese).

Guo, R., Bu, A., 2006. New discovery and understanding about seeking the copper-lead-zinc polymetallic deposits in volcanic basin of East Guangdong. Miner. Resour. Geol. 20, 243–245 (in Chinese with English abstract).

Guo, F., Fan, W.M., Li, C.W., Zhao, L., Li, H.X., Yang, J.H., 2012. Multi-stage crust–mantle interaction in SE China: temporal, thermal and compositional constraints from the Mesozoic felsic volcanic rocks in eastern Guangdong–Fujian provinces. Lithos 150, 62–84.

Harris, N.B., Pearce, J.A., Tindle, A.G., 1986. Geochemical characteristics of collision-zone magmatism. Geol. Soc. Lond., Spec. Publ. 19, 67–81.

He, Z.Y., Xu, X.S., 2012. Petrogenesis of the Late Yanshanian mantle-derived intrusions in southeastern China: response to the geodynamics of paleo-Pacific plate subduction. Chem. Geol. 328, 208–221.

Heinrich, C.A., 1990. The chemistry of hydrothermal tin (-tungsten) ore deposition. Econ. Geol. 85, 457–481.

Hoskin, P.W.O., Schaltegger, U., 2003. The composition of zircon and igneous and metamorphic petrogenesis. Rev. Mineral. Geochem. 53, 27–62.

Hu, R.Z., Zhou, M.F., 2012. Multiple Mesozoic mineralization events in South China—an introduction to the thematic issue. Mineral. Deposita 47, 579–588.

Hua, R.M., Chen, P.R., Zhang, W.L., Lu, J.J., 2005. Three major metallogenic events in Mesozoic in South China. Mineral Deposits 24, 99–107 (in Chinese with English abstract).

Hua, R.M., Li, G.L., Zhang, W.L., Hu, D.Q., Chen, P.R., Chen, W.F., Wang, X.D., 2010. A tentative discussion on differences between large-scale tungsten and tin mineralizations in South China. Mineral Deposits 29, 9–23 (in Chinese with English abstract).

Jiang, S.Y., Li, L., Zhu, B., Ding, X., Jiang, Y.H., Gu, L.X., Ni, P., 2008. Geochemical and Sr-Nd-Hf isotopic compositions of granodiorite from the Wushan copper deposit, Jiangxi Province and their implications for petrogenesis. Acta Petrol. Sin. 24, 1679–1690 (in Chinese with English abstract).

Jiang, Y.H., Zhao, P., Zhou, Q., Liao, S., Jin, G., 2011. Petrogenesis and tectonic implications of Early Cretaceous S- and A-type granites in the northwest of the Gan-Hang rift, SE China. Lithos 121, 55–73.

Jiang, Y.H., Wang, G.C., Liu, Z., Ni, C.Y., Qing, L., Zhang, Q., 2015. Repeated slab advance–retreat of the Palaeo-Pacific plate underneath SE China. Int. Geol. Rev. 57, 472–491.

Karsli, O., Dokuz, A., Uysal, I., Aydin, F., Chen, B., Kandemir, R., Wijbrans, J., 2010. Relative contributions of crust and mantle to generation of Campanian high-K calc-alkaline I-type granitoids in a subduction setting, with special reference to the Harşit Pluton, eastern Turkey. Contrib. Mineral. Petrol. 160, 467–487.

Lapierre, H., Jahn, B.M., Charvet, J., Yu, Y.W., 1997. Mesozoic felsic arc magmatism and continental olivine tholeiites in Zhejiang Province and their relationship with the tectonic activity in southeastern China. Tectonophysics 274, 321–338.

Lehmann, B., Harmanto, 1990. Large-scale tin depletion in the Tanjungpandan tin granite, Belitung Island, Indonesia. Econ. Geol. 85, 99–111.

Lei, X.Y., Yue, S.C., 1993. Studies on geochemical features and genesis of the granitoids in eastern Guangdong. Resour. Surv. Environ. 14, 13–22 (in Chinese with English abstract).

Li, Z.X., Li, X.H., 2007. Formation of the 1300-km-wide intracontinental orogen and postorogenic magmatic province in Mesozoic South China: a flat-slab subduction model. Geology 35, 179–182.

Li, X.H., Li, Z.X., Zhou, H.W., Liu, Y., Kinny, P.D., 2002. U–Pb zircon geochronology, geochemistry and Nd isotopic study of Neoproterozoic bimodal volcanic rocks in the Kangdian Rift of South China: implications for the initial rifting of Rodinia. Precambrian Res. 113, 135–154.

Li, X.H., Li, Z.X., Ge, W.C., Zhou, H.W., Li, W.X., Liu, Y., Wingate, M.T.D., 2003. Neoproterozoic granitoids in South China: crustal melting above a mantle plume at ca. 825 Ma? Precambrian Res. 122, 45–83.
Li, H.Q., Lu, Y.F., Wang, D.H., Chen, Y.C., Yang, H.M., Guo, J., Xie, C.F., Yang, Y.P., Ma, L.Y., 2006. Dating of the rock-forming and ore-forming ages and their geological significances in the Furong ore-field, Qitian Mountain, Hunan. Geol. Rev. 52, 113–121 (in Chinese with English abstract).
Li, X.H., Li, Z.X., Li, W.X., 2007a. U–Pb zircon, geochemical and Sr–Nd–Hf isotopic constrains on age and origin of Jurassic I- and A-type granites from Central Guangdong, SE China: a major igneous event in response to foundering of a subducted flat-slab? Lithos 96, 186–204.
Li, X.H., Li, W.X., Li, Z.X., 2007b. On the genetic classification and tectonic implications of the Early Yanshanian granitoids in the Nanling Range, South China. Chin. Sci. Bull. 52, 1873–1885.
Li, X.H., Long, W.W., Li, Q.L., Liu, Y., Zheng, Y.F., Yang, Y., Chamberlain, K.R., Wan, D., Guo, C., Wang, X., 2010. Penglai zircon megacrysts: a potential new working reference material for microbeam determination of Hf–O isotopes and U–Pb age. Geostand. Geoanal. Res. 34, 117–134.
Li, H., Zhang, H., Ling, M.X., Wang, F.Y., Ding, X., Zhou, J.B., Yang, X.Y., Tu, X.L., Sun, W.D., 2011. Geochemical and zircon U-Pb study of the Huangmeijian A-type granite: implications for geological evolution of the Lower Yangtze River belt. Int. Geol. Rev. 53, 499–525.
Li, S.S., Chen, S.Q., Bu, A., 2012. Geology, geochemistry and genesis of the Jinkeng Sn polymetallic deposit, Guangdong Province. Adv. Earth Sci. 27, 212–215 (in Chinese with English abstract).
Li, B., Jiang, S.Y., Zhang, Q., Zhao, H.X., Zhao, K.D., 2015. Cretaceous crust–mantle interaction and tectonic evolution of Cathaysia block in South China: evidence from pulsed mafic rocks and related magmatism. Tectonophysics 661, 136–155.
Li, H.L., Xiao, H.L., Fan, F.P., Chen, L.Z., Liu, J.X., Chen, X.T., 2016. Molybdenite Re–Os isotopic age of Fei'eshan tungsten and molybdenum polyetallic deposit in Chao'an, Guangdong. Acta Geol. Sin. 90, 231–239 (in Chinese with English abstract).
Lin, W.W., Peng, L.J., 1994. The estimation of Fe^{3+} and Fe^{2+} contents in amphibole and biotite from EPMA data. J. Changchun Univ. Sci. Technol. 24, 155–162 (in Chinese with English abstract).
Linnen, R.L., Pichavant, M., Holtz, F., 1996. The combined effects of f_{O2} and melt composition on SnO_2 solubility and tin diffusivity in haplogranitic melts. Geochim. Cosmochim. Acta 60, 4965–4976.
Liu, Y.S., Gao, S., Hu, Z.C., Gao, C.G., Zong, K.Q., Wang, D.B., 2010. Continental and oceanic crust recycling-induced melt–peridotite interactions in the trans-North China orogen: U–Pb dating, Hf isotopes and trace elements in zircons from mantle xenoliths. J. Petrol. 51, 537–571.
Liu, P., Cheng, Y.B., Mao, J.W., Wang, X.Y., Yao, W., Cheng, X.T., Zeng, X.J., 2015. Zircon U–Pb age and Hf isotopic characteristics of granite from the Tiandong W-Sn polymetallic deposit in eastern Guangdong Province and its significance. Acta Geol. Sin. 89, 1244–1257 (in Chinese with English abstract).
Liu, L., Xu, X., Xia, Y., 2016. Asynchronizing paleo-Pacific slab rollback beneath SE China: insights from the episodic Late Mesozoic volcanism. Gondwana Res. 37, 397–407.
Ludwig, K.R., 2003. User's Manual for Isoplot/Ex Version 3.00—A Geochronology Toolkit for Microsoft Excel. 4. Berkeley Geochronol. Cent. Spec. Publ., pp. 1–70.
Mao, J.W., Xie, G.Q., Li, X.F., Zhang, C.Q., Mei, Y.X., 2004. Mesozoic large-scale mineralization and multiple lithospheric extensions in South China. Earth Sci. Front. 11, 45–55 (in Chinese with English abstract).
Mao, J.W., Xie, G.Q., Guo, C.L., Yuan, S.D., Cheng, Y.B., Chen, Y.C., 2008. Spatial–temporal distribution of Mesozoic ore deposits in South China and their metallogenic settings. Geol. J. China Univ. 14, 510–526 (in Chinese with English abstract).
Mao, J.W., Cheng, Y.B., Chen, M.H., Pirajno, F., 2013a. Major types and time–space distribution of Mesozoic ore deposits in South China and their geodynamic settings. Mineral. Deposita 48, 267–294.
Mao, Z.H., Cheng, Y.B., Liu, J.J., Yuan, S.D., Wu, S.H., Xiang, X.K., Luo, X.H., 2013b. Geology and molybdenite Re–Os age of the Dahutang granite-related veinlets-disseminated tungsten ore field in the Jiangxi Province, China. Ore Geol. Rev. 53, 422–433.
Ni, S.B., Man, F.S., Bai, Y.Z., Li, T., 1983. Rr–Sr dating of Lianhuashan tungsten ore deposit. J. China Univ. Sci. Technol. 13, 246–252 (in Chinese with English abstract).
Pearce, J.A., 1996. Sources and settings of granitic rocks. Episodes 19, 120–125.
Peccerillo, A., Taylor, S.R., 1976. Geochemistry of Eocene calc-alkaline volcanic rocks from the Kastamonu area, northern Turkey. Contrib. Mineral. Petrol. 58, 63–81.
Pitcher, W.S., 1987. Granites and yet more granites forty years on. Geol. Rundsch. 76, 51–79.
Qiu, Y.X., Qiu, J.S., Li, J.C., Zhong, H.P., 1991. Deformational and metamorphic features of Lianhuashan fault zone during Mesozoic time and mechanism of their formation. J. Geomech. 14, 93–106 (in Chinese with English abstract).
Qiu, J.S., Hu, J., Wang, X.L., Jiang, S.Y., Wang, R.C., Xu, X.S., 2005. The Baishigang Pluton in Heyuan, Guangdong Province: a highly fractionated I-type granite. Acta Geol. Sin. 79, 503 (in Chinese with English abstract).
Qiu, Z.W., Wang, H., Wang, L.M., Bu, A., Li, S.S., Mu, S.L., Li, P., Wei, X.P., 2016a. Zircon U–Pb geochronology, geochemistry and Lu–Hf isotopes of the granite porphyry in the Taoxihu tin polymetallic deposit, Guangdong Province, SE China and its geological significance. Geotecton. Metallog. http://cnki.net/kcms/doi/10.16539/j.ddgzyckx.2016.05.016.html (in Chinese with English abstract).
Qiu, Z.W., Wang, H., Yan, Q.H., Li, S.S., Wang, L.M., Bu, A., Mu, S.L., Li, P., Wei, X.P., 2016b. Zircon U–Pb geochronology and Lu–Hf isotopes of the quartz porphyry in the Changpu Sn polymetallic deposit, Guangdong Province, SE China and its geological significance. Geochemica 45, 374–386 (in Chinese with English abstract).
Roberts, M.P., Clemens, J.D., 1993. Origin of high-potassium, talc-alkaline, I-type granitoids. Geology 21, 825–828.
Rubatto, D., Gebauer, D., 2000. Use of cathodoluminescence for U–Pb zircon dating by ion microprobe: some examples from the Western Alps. Cathodoluminescence in Geosciences. Springer, Berlin Heidelberg, pp. 373–400.
Shu, X.J., Wang, X.L., Sun, T., Xu, X., Dai, M.N., 2011. Trace elements, U–Pb ages and Hf isotopes of zircons from Mesozoic granites in the western Nanling Range, South China: implications for petrogenesis and W–Sn mineralization. Lithos 127, 468–482.
Söderlund, U., Patchett, P.J., Vervoort, J.D., Isachsen, C.E., 2004. The ^{176}Lu decay constant determined by Lu–Hf and U–Pb isotope systematics of Precambrian mafic intrusions. Earth Planet. Sci. Lett. 219, 311–324.
Sun, S.S., McDonough, W.E., 1989. Chemical and isotopic systematics of oceanic basalts: implications for mantle composition and processes. In: Saunders, A.D., Norry, M.J. (Eds.), Magmatism in the Ocean Basins: Geological Society of London. Special Publication 42, pp. 313–345.
Sun, Y.L., Xu, P., Li, J., He, K., Chu, Z.Y., Wang, C.Y., 2010. A practical method for determination of molybdenite Re–Os age by inductively coupled plasma-mass spectrometry combined with Carius tube-HNO_3 digestion. Anal. Methods 2, 575–581.
Sun, F.J., Xu, X.S., Zou, H.B., Xia, Y., 2015. Petrogenesis and magmatic evolution of ~130 Ma A-type granites in Southeast China. J. Asian Earth Sci. 98, 209–224.
Sylvester, P.J., 1998. Postcollisional strongly peraluminous granites. Lithos 45, 29–44.
Tao, J.H., Li, W.X., Li, X.H., Cen, T., 2013. Petrogenesis of Early Yanshanian highly evolved granites in the Longyuanba area, southern Jiangxi Province: evidence from zircon U–Pb dating, Hf–O isotope and whole-rock geochemistry. Sci. China Earth Sci. 56, 922–939.
Taylor, S.R., Mclennan, S.M., 1985. The Continental Crust: Its Composition and Evolution. Blackwell, London, pp. 1–312.
Teixeira, R.J.S., Neiva, A.M.R., Gomes, M.E.P., Corfu, F., Cuesta, A., Croudace, I., 2012. The role of fractional crystallization in the genesis of early syn-D_3, tin-mineralized Variscan two-mica granites from the Carrazeda de Ansiães area, northern Portugal. Lithos 153, 177–191.
Topuz, G., Altherr, R., Siebel, W., Schwarz, W.H., Zack, T., Hasözbek, A., Barth, M., Satir, M., Şen, C., 2010. Carboniferous high-potassium I-type granitoid magmatism in the eastern Pontides: the Gümüşhane pluton (NE Turkey). Lithos 116, 92–110.
Wang, R.C., Xie, L., Chen, J., Yu, A., Wang, L., Lu, J., Zhu, J., 2013. Tin-carrier minerals in metaluminous granites of the western Nanling Range (southern China): constraints on processes of tin mineralization in oxidized granites. J. Asian Earth Sci. 74, 361–372.
Watson, E.B., Harrison, T.M., 1983. Zircon saturation revisited: temperature and composition effects in a variety of crustal magma types. Earth Planet. Sci. Lett. 64, 295–304.
Whalen, J.B., Currie, K.L., Chappell, B.W., 1987. A-type granites: geochemical characteristics, discrimination and petrogenesis. Contrib. Mineral. Petrol. 95, 407–419.
Wones, D.R., Eugster, H.P., 1965. Stability of biotite-experiment theory and application. Am. Mineralist 50, 1228–1272.
Wong, J., Sun, M., Xing, G.F., Li, X.H., Zhao, G.C., Wong, K., Yuan, C., Xia, X.P., Li, L.M., Wu, F.Y., 2009. Geochemical and zircon U–Pb and Hf isotopic study of the Baijuhuajian metaluminous A-type granite: extension at 125–100 Ma and its tectonic significance for South China. Lithos 112, 289–305.
Wu, Y.B., Zheng, Y.F., 2004. The genesis of zircon and the constraints on the interpretation of U-Pb age. Chin. Sci. Bull. 49, 1589–1604 (in Chinese with English abstract).
Wu, F.Y., Jahn, B.M., Wilde, S.A., Lo, C.H., Yui, T.F., Lin, Q., Sun, D.Y., 2003a. Highly fractionated I-type granites in NE China (I): geochronology and petrogenesis. Lithos 66, 241–273.
Wu, F.Y., Jahn, B.M., Wilde, S.A., Lo, C.H., Yui, T.F., Lin, Q., Sun, D.Y., 2003b. Highly fractionated I-type granites in NE China (II): isotopic geochemistry and implications for crustal growth in the Phanerozoic. Lithos 67, 191–204.
Wu, F.Y., Yang, Y.H., Xie, L.W., Yang, J.H., Xu, P., 2006. Hf isotopic compositions of the standard zircons and baddeleyites used in U–Pb geochronology. Chem. Geol. 234, 105–126.
Wu, F.Y., Li, X.H., Yang, J.H., Zheng, Y.F., 2007. Discussions on the petrogenesis of granites. Acta Petrol. Sin. 23, 1217–1238 (in Chinese with English abstract).
Wyborn, D., Chappell, B.W., James, M., 2001. Examples of convective fractionation in high temperature granites from the Lachlan Fold Belt. Aust. J. Earth Sci. 48, 531–541.
Xiong, X.L., Adam, J., Green, T.H., 2005. Rutile stability and rutile/melt HFSE partitioning during partial melting of hydrous basalt: implications for TTG genesis. Chem. Geol. 218, 339–359.
Xu, X.C., 1993. Geochemical Studies on the Mesozoic Magmatic and Metallization, Eastern Guangdong Province, China. (Ph.D. Thesis). Hefei University of Technology, Hefei, pp. 1–187 (in Chinese with English abstract).
Xu, X.C., Yue, S.C., 1999a. Source material and metallization of tin (tungsten, copper) polymetallic deposits in eastern Guangdong Province. J. Hefei Univ. Technol. 34, 81–92 (in Chinese with English abstract).
Xu, X.C., Yue, S.C., 1999b. Continental crust anatexite: the genesis of Mesozoic granitic volcanic–intrusive complexes, eastern Guangdong Province—constraints on Pb–Nd–Sr multi-element isotopic systems. Geol. Rev. 45, 829–835 (in Chinese with English abstract).
Xu, X.C., Xie, Q.Q., Yue, S.C., 2000. Mesozoic volcanic and intrusive rocks in eastern Guangdong province, China: genesis, types and petrologic implication. Sci. Geol. Sin. 9, 253–262.
Xu, X.S., O'Reilly, S.Y., Griffin, W.L., Wang, X.L., Pearson, N.J., He, Z.Y., 2007. The crust of Cathaysia: age, assembly and reworking of two terranes. Precambrian Res. 158, 51–78.
Xu, B., Jiang, S.Y., Wang, R., Ma, L., Zhao, K.D., Yan, X., 2015. Late Cretaceous granites from the giant Dulong Sn-polymetallic ore district in Yunnan Province, South China: geochronology, geochemistry, mineral chemistry and Nd–Hf isotopic compositions. Lithos 218–219, 54–72.
Xu, B., Jiang, S.Y., Luo, L., Zhao, K.D., Ma, L., 2016. Origin of the granites and related Sn and Pb-Zn polymetallic ore deposits in the Pengshan district, Jiangxi Province, South China: constraints from geochronology, geochemistry, mineral chemistry, and Sr–

Nd–Hf–Pb–S isotopes. Mineral. Deposita http://dx.doi.org/10.1007/s00126-016-0659-7.

Yan, X., Jiang, S.Y., Jiang, Y.H., 2015. Geochronology, geochemistry and tectonic significance of the late Mesozoic volcanic sequences in the northern Wuyi Mountain volcanic belt of South China. Gondwana Res. 37, 362–383.

Yang, S.Y., Jiang, S.Y., Jiang, Y.H., Zhao, K.D., Fan, H.H., 2011. Geochemical, zircon U–Pb dating and Sr–Nd–Hf isotopic constraints on the age and petrogenesis of an Early Cretaceous volcanic-intrusive complex at Xiangshan, Southeast China. Mineral. Petrol. 101, 21–48.

Yang, S.Y., Jiang, S.Y., Zhao, K.D., Jiang, Y.H., Ling, H.F., Luo, L., 2012. Geochronology, geochemistry and tectonic significance of two Early Cretaceous A-type granites in the Gan-Hang Belt, Southeast China. Lithos 150, 155–170.

Zhang, W.L., Hua, R.M., Wang, R.C., Chen, P.R., Li, H.M., 2006. New dating of the Dajishan granite and related tungsten mineralization in southern Jiangxi. Acta Geol. Sin. 80, 956–962 (in Chinese with English abstract).

Zhang, Y., Yang, J.H., Sun, J.F., Zhang, J.H., Chen, J.Y., Li, X.H., 2015. Petrogenesis of Jurassic fractionated I-type granites in Southeast China: constraints from whole-rock geochemical and zircon U–Pb and Hf–O isotopes. J. Asian Earth Sci. 111, 268–283.

Zhao, X.L., Yu, M.G., Liu, K., Mao, J.R., Ye, H.M., Xing, G.F., 2012. The magmatic and genetic evolution of Early Cretaceous granitoids in eastern Guangdong Province. Geol. Rev. 58, 965–977 (in Chinese with English abstract).

Zhou, X.M., Li, W.X., 2000. Origin of late Mesozoic igneous rocks in southeastern China: implications for lithosphere subduction and underplating of mafic magmas. Tectonophysics 326, 269–287.

Zhou, X.M., Sun, T., Shen, W.Z., Shu, L.S., Niu, Y.L., 2006. Petrogenesis of Mesozoic granitoids and volcanic rocks in South China: a response to tectonic evolution. Episodes 29, 26–33.

Zhou, Z.M., Ma, C.Q., Xie, C.F., Wang, L.X., Liu, Y.Y., Liu, W., 2016. Genesis of highly fractionated I-type granites from Fengshun complex: implications to tectonic evolutions of South China. J. Earth Sci. 27, 444–460.

Zhu, J.C., Zhang, P.H., Xie, C.F., Zhang, H., Yang, C., 2006. Zircon U–Pb age framework of Huashan–Guposhan intrusive belt, western part of Naniing Range, and its geological significance. Acta Petrol. Sin. 22, 2270–2278 (in Chinese with English abstract).